Nemo-like kinase disrupts nuclear import and drives TDP43 mislocalization in ALS

Michael E. Bekier II[1#], Emile Pinarbasi[1,2#], Jack J. Mesojedec[1], Layla Ghaffari[3], Martina de Majo[3], Erik Ullian[4], Mark Koontz[3], Sarah Coleman[3], Xingli Li[1], Elizabeth M. H. Tank[1], Jacob Waksmacki[1], Sami Barmada[1]*

[1]Department of Neurology, University of Michigan, Ann Arbor, MI, 48109, United States

[2]Department of Pathology, Michigan Medicine, University of Michigan, Ann Arbor, MI, 48109, United States

[3]Synapticure, Chicago, IL, United States 60612

[4]Department of Ophthalmology & Physiology, University of California San Francisco, San Francisco, CA, 94143, United States

# contributed equally

*Correspondence to Sami Barmada: 109 Zina Pitcher Place, Ann Arbor, MI, 48019; 734-764-8425; sbarmada@umich.edu

Conflict of Interest Statement:

S.J.B. serves on the advisory board for Neurocures, Inc., Symbiosis, Eikonizo Therapeutics, 15 Ninesquare Therapeutics, the Live Like Lou Foundation, Synapticure, and the Robert Packard

Center for ALS Research. S.J.B. has received research funding from Denali Therapeutics, Biogen, Inc., Lysoway Therapeutics, Amylyx Therapeutics, Acelot Therapeutics, Meira GTX, Inc., Prevail Therapeutics, Eikonizo Therapeutics, and Ninesquare Therapeutics.

Abstract

Cytoplasmic TDP43 mislocalization and aggregation are pathological hallmarks of amyotrophic lateral sclerosis (ALS). However, the initial cellular insults that lead to TDP43 mislocalization remain unclear. In this study, we demonstrate that Nemo-like kinase (NLK)—a proline-directed serine/threonine kinase—promotes the mislocalization of TDP43 and other RNA-binding proteins by disrupting nuclear import. NLK levels are selectively elevated in neurons exhibiting TDP43 mislocalization in ALS patient tissues, while genetic reduction of *NLK* reduces toxicity in human neuron models of ALS. Our findings suggest that NLK is a promising therapeutic target for neurodegenerative diseases.

33 **Introduction**

34 Amyotrophic lateral sclerosis (ALS) is a fatal and progressive neurodegenerative disease
35 distinguished by loss of motor neurons in the cortex and spinal cord (1). The clinical presentation of
36 ALS is heterogeneous, depending in large part upon the neuroanatomical pathways involved.
37 Despite this, a single pathological hallmark — mislocalization and aggregation of the RNA binding
38 protein TDP43 — is found in >95% of individuals (2).

39 TDP43 is crucial for several aspects of RNA processing, including RNA splicing, stability and
40 transport (3-7). TDP43 is primarily nuclear in healthy cells, in contrast to the nuclear exclusion and
41 cytosolic deposition of TDP43 that are characteristic of ALS (3). Although the origins of TDP43
42 mislocalization are unclear, deficiencies in nucleocytoplasmic transport machinery are
43 increasingly implicated as a potential contributing factor to ALS pathology (8). Impaired nuclear
44 import of TDP43 and other RNA binding proteins, together with dysfunction of the nuclear pore
45 complex itself, are observed in human induced pluripotent stem cell (iPSC)-derived neurons from
46 sporadic and familial ALS patients as well as post-mortem samples. Genetic screens in ALS model
47 systems have repeatedly uncovered nuclear pore and nucleocytoplasmic transport factors as
48 potent disease modifiers, confirming the significance of these pathways in disease pathogenesis
49 (9-11).

50 Among the most consistent and dramatic disease modifiers to emerge from these screens is
51 nemo-like kinase (NLK), a proline directed serine-threonine kinase that regulates cell
52 differentiation (12), proliferation, and apoptosis (13, 14). NLK depletion mitigates disease
53 phenotypes not just in *Drosophila* and murine models of ALS, but also murine models of
54 spinobulbar muscular atrophy, and murine models of spinocerebellar ataxia (15-17). Conversely,

55 NLK overexpression reduces toxicity in Huntington's disease models, indicating context-dependent
56 effects of NLK in neurodegeneration (18).

57 NLK has several predicted substrates that function in nucleocytoplasmic transport, but whether
58 NLK itself may influence nuclear import and ALS pathogenesis remains unknown. Here, we
59 demonstrate that NLK is a pivotal regulator of nucleocytoplasmic transport. NLK accumulation
60 leads directly to the cytoplasmic accumulations of TDP43 and other RNA-binding proteins
61 associated with ALS, while reduction in NLK promotes the survival of iPSC-derived neurons
62 carrying ALS-associated mutations. Importantly, NLK is upregulated selectively in affected neurons
63 from ALS patients and correlates with TDP43 mislocalization, implicating NLK as a key determinant
64 of disease pathophysiology and highlighting NLK as a promising therapeutic target for ALS and
65 related TDP43 proteinopathies.

66

67 **Results**

68 **NLK overexpression drives mislocalization of TDP43 and other ALS-linked RNA-binding**
69 **proteins**

70 To determine if NLK is capable of directly influencing TDP43 localization, we transfected HEK293
71 cells with plasmids encoding FLAG-tagged wild-type (WT) NLK and examined TDP43 localization by
72 immunofluorescence (Figure 1A). Exogenous NLK, like endogenous NLK, is both cytoplasmic and
73 nuclear in distribution (19). As a control, we also transfected cells with plasmids encoding FLAG-
74 tagged kinase-negative (KN) NLK, which harbors a point mutation in the active site (K155M) that
75 abrogates kinase activity (19). NLK WT overexpression significantly decreased the nuclear-
76 cytoplasmic (NC) ratio of endogenous TDP43 compared to NLK KN (Figure 1B). The change in

77 TDP43 NC ratio was driven by both a reduction in nuclear TDP43 as well as a concordant increase
78 in cytoplasmic TDP43, consistent with nuclear-cytoplasmic TDP43 mislocalization (Figure 1C-D).

79 We next asked whether NLK WT solely affected TDP43 localization, or whether it also regulated the
80 distribution of other ALS-associated RNA binding proteins that undergo nucleocytoplasmic
81 transport, including HNRNPA2B1 and Matrin-3. We also examined the localization of FUS, an RNA
82 binding protein harboring a non-classical PY-nuclear localization signal (NLS) recognized by
83 importin-$ß_2$, in contrast to the classical K/R-rich NLS in TDP43, HNRNPA2B1, and MATR3 that binds
84 importin-α (20-22). As before, HEK293 cells were transfected with KN or WT NLK, and the
85 subcellular distribution of each protein determined by immunofluorescence (Figure 1F-K).
86 Compared to NLK KN, NLK WT overexpression significantly reduced the NC ratio of both FUS and
87 HNRNPA2B1 but had no significant effect on Matrin-3 localization (Figure 1F-K). Together, these
88 findings suggest that WT NLK overexpression disrupts nuclear localization of multiple RNA-binding
89 proteins harboring classical as well as non-classical NLSs, in a kinase-dependent manner.

90

91 **NLK overexpression disrupts nuclear import**

92 At steady state, nuclear localization of TDP43 and other RNA-binding proteins is maintained
93 through two competing processes: active nuclear import and passive efflux through the nuclear
94 pore (23-25). To directly evaluate nuclear import, we co-expressed NLK together with YFP fusion
95 proteins containing NLS sequences from TDP43 (YFP-NLS^{TDP}), FUS (YFP-NLS^{FUS}), Matrin-3 (YFP-
96 NLS^{MATR3}) and SV40 (YFP-NLS^{SV40}, a canonical classical NLS) followed by immunofluorescence for
97 TDP43, FUS, or Matrin-3 (Figures 2A-H). Notably, WT NLK expression drives mislocalization of YFP-
98 NLS^{MATR3}, but not endogenous Matrin-3 (Figure 1J, K), potentially due to the relatively large size of
99 Matrin-3 (95kDa, vs 27kDa for YFP-NLS^{MATR3}) (23, 24). Compared to overexpression of NLK KN, NLK

100 WT significantly increased the NC ratio of all NLS-fusion proteins (Figure 2C). Similar to what we
101 observed for native RNA binding proteins (Figure 1), WT NLK affects reporters containing both
102 classical as well as non-classical NLS motifs (26). Collectively, these data indicate that WT NLK
103 overexpression disrupts global nuclear import through its kinase activity.

104

105 **NLK-induced TDP43 mislocalization is independent of KPNA2 nuclear accumulation**

106 Nuclear import relies on transport receptor proteins, such as KPNA2 and KPNB1, which recognize
107 and bind to NLS-containing proteins such as TDP43 (27). Thus, we examined the sub-cellular
108 localization of KPNB1 and KPNA2 by immunofluorescence after overexpression of either KN or WT
109 NLK. Overexpression of WT NLK significantly increased the NC ratio of both KPNA2 and KPNB11,
110 driven by a significant increase in their nuclear fractions without a corresponding decrease in their
111 cytoplasmic abundance (Figure 3A-D, S1A-B). Because of the critical importance of these factors
112 for nuclear import, we questioned whether the mislocalization of TDP43 and other RNA binding
113 proteins may be secondary to the observed nuclear accumulation of KPNA2 and/or KPNB1. To test
114 this hypothesis, we took advantage of previous data showing that nuclear accumulation of KPNA2
115 can be reversed by the expression of the E3 ubiquitin ligase FBXW7 (28). HEK293 cells were
116 transfected with plasmids encoding FLAG-tagged NLK WT and either mApple (negative control) or
117 FBXW7 followed by immunofluorescence for KPNA2 (Figure 3E, F). Compared to mApple, FBXW7-
118 V5 significantly reduced the NC ratio of KPNA2 in NLK-overexpressing cells (Figure 3G), due
119 primarily to reduction in the nuclear KPNA2signal (Figure 3D, S1C). Despite this, FBXW7-V5
120 coexpression failed to significantly correct TDP43 mislocalization in cells transfected with WT NLK
121 (Figure 3G, H, S1D). These results indicate that NLK-induced mislocalization of TDP43 does not
122 depend on the nuclear accumulation of KPNA2.

123

124 **NLK overexpression promotes mislocalization of Ran, Ran-GAP1, and RanBP2**

125 Nuclear localization of receptor-bound cargo is mediated by RanGAP1 and RanBP2, nuclear pore-
126 associated factors that regulate the Ran gradient (29)(Figure S2). Consistent with a previous screen
127 for kinase-interacting proteins (30), both RanGAP1 and RanBP2 co-immunoprecipitated with FLAG-
128 NLK in HEK293 cells (Figure 4A-C). NLK overexpression also promoted the accumulation of non-
129 sumoylated RanGAP1 (Figure 4A). RanGAP1 sumoylation is critical for nuclear envelope
130 localization and its interaction with RanBP2 (Figure 4 C, (31-33)). This prompted us to investigate
131 the impact of NLK overexpression on the subcellular localization of RanGAP1, RanBP2, and
132 ultimately Ran. Compared to KN NLK overexpression, WT NLK significantly disrupted the expected
133 nuclear envelope localization of RanGAP1 and RanBP2 as measured by the ratio of nuclear rim
134 density to cytoplasmic density (Figure 4D-G). Conversely, overexpression of NLK WT did not
135 significantly impact FG nucleoporins as detected by MAb414 (Figure 4H, I). WT NLK overexpression
136 also reduced the NC ratio of Ran, driven by both a decrease in nuclear Ran and an increase in
137 cytoplasmic Ran (Figure 4J, K). As such, NLK-induced disruption of the Ran gradient correlates with
138 disruption of the RanGAP1-RanBP2 complex and impaired nucleocytoplasmic transport.

139

140 **NLK drives redistribution of mRNA and disassembles nuclear speckles**

141 The localization of TDP43 and other RNA-binding proteins is heavily influenced not just by their NLS
142 motifs, but also by their cognate RNA substrates (34). Based on this, we examined whether TDP43
143 mislocalization upon WT NLK overexpression is RNA-dependent. Initially, we transfected HEK293
144 cells with an EGFP-tagged variant of TDP43 harboring two mutations within RRM1 that abolish RNA
145 binding, TDPF2L-EGFP (F147L/F149L)(35, 36) , together with WT or KN NLK (Figure 5A). TDPF2L-

146 EGFP formed phase-separated droplets that were largely restricted to the nucleus in cells co-
147 expressing KN NLK, as in prior studies (37). However, co-transfection with WT NLK resulted in the
148 appearance of cytosolic TDP43F2L-EGFP droplets, suggesting that TDP43 mislocalization upon WT
149 NLK overexpression is independent of RNA binding (Figure 5A and S3A).

150 We also investigated whether WT NLK overexpression could affect the distribution of
151 polyadenylated (polyA) mRNA. We first immunostained for NXF1, an mRNA export factor which
152 itself contains a PY-NLS (20) and saw that in NLK WT transfected cells, NXF1 accumulates in the
153 cytoplasm (Figure 5B and S3B). Next, we directly assessed mRNA distribution using fluorescence
154 in-situ hybridization (FISH). While untransfected and KN NLK-expressing cells displayed a punctate
155 pattern of polyA mRNA within the nucleus, WT NLK overexpression resulted in a more diffuse and
156 evenly distributed nuclear signal, and minimal changes in the polyA mRNA NC ratio (Figure 5C and
157 S4C). Given the enrichment of polyA mRNA within nuclear speckles, and the apparent loss of such
158 structures with WT NLK overexpression, we also immunostained WT or KN NLK-transfected cells
159 using the SC35 antibody, which recognizes SRRM2, a core component of nuclear speckles (38). WT
160 NLK-expressing cells, in contrast to untransfected or KN NLK-transfected cells, displayed a
161 dramatic reduction in nuclear speckles (Figure 5D). This effect appeared to be specific for nuclear
162 speckles, as we saw no change in other nuclear membraneless organelles such as paraspeckles
163 (marked by SFPQ (39); Figure 5E) or nucleoli (marked by nucleophosmin (40); Figure 5F) in WT NLK-
164 expressing cells.

165

166 **NLK overexpression disrupts nuclear import in mammalian neurons**

167 To examine the impact of NLK overexpression on RBPs and nuclear import factors in neurons, we
168 transfected rodent primary mixed cortical neurons with either SNAP-FLAG (SF; negative control) or

169 SNAP-FLAG-NLK WT (SF-NLK) before immunostaining for TDP43 and other factors affected by NLK.
170 Consistent with our results in HEK293 cells, expression of SF-NLK but not SF significantly impacted
171 the subcellular localization of TDP43, FUS, RanGAP1, RanBP2, and Ran (Figure 6A-D). As before,
172 the central channel of the NPC marked by FG nucleoporins was unaffected by SF-NLK expression
173 (Figure 6E), while exogenous reporters such as YFP-NLS^{SV40} were mislocalized by SF-NLK but not SF
174 in transfected neurons (Figure S4).

175 Nucleocytoplasmic trafficking is essential for maintaining protein and RNA homeostasis; thus, we
176 predicted that NLK-induced disruption of nucleocytoplasmic transport would lead to substantial
177 toxicity. To assess this, we utilized automated longitudinal microscopy to track hundreds of rodent
178 primary mixed cortical neurons cultures prospectively for 10 days in culture. Neurons were
179 transfected with SF or SF-NLK, in combination with a survival marker (GFP) enabling us to
180 determine the time of cell death (Figure 6F, G). SF-NLK overexpression significantly increased the
181 cumulative risk of death in transfected neurons compared to SF alone (HR=1.61, $p<0.001$, Cox
182 proportional hazards analysis; Figure 6H). Since all data on survival are acquired from individual
183 neurons, and the abundance of fluorescently-tagged proteins is directly proportional to the
184 measured signal intensity (41), we investigated the relationship between SNAP-FLAG-NLK intensity
185 and the hazard of the event using a Cox proportional hazards model with penalized splines (42-44).
186 The Cox model revealed significant non-linear relationships between signal intensity and hazard,
187 as indicated by a Likelihood Ratio Test statistic of χ^2 (4.06) = 25.89 ($p < 0.0001$), suggesting that the
188 model fits the data well. The concordance index was 0.587, indicating a moderate ability of the
189 model to discriminate between different hazard levels. Hazard ratios were calculated for distinct
190 intensity segments derived from the spline model. For low signal intensities, the hazard ratio was
191 0.898 (95% CI: 0.378 - 2.132), indicating a slight decrease in hazard compared to the baseline. In
192 the medium intensity range, the hazard ratio increased to 1.555 (95% CI: 0.532 - 4.545), suggesting

193 a potential increase in risk. Notably, for high signal intensities, the hazard ratio rose significantly to
194 4.629 (95% CI: 0.701 - 30.584), reflecting a substantial elevation in hazard associated with
195 increased signal intensity (Figure 6I). Collectively, our data indicate that overexpression of NLK
196 significantly impairs the mechanisms that regulate nucleocytoplasmic transport, leading to the
197 mislocalization of pertinent RNA-binding proteins and ultimately neuron death.

198

199 **Increased NLK levels correlate with TDP43 pathology in disease models and patients**

200 Approximately 50% of individuals with frontotemporal lobar degeneration (FTLD) show TDP43
201 mislocalization as in ALS(3). In addition, up to half of people with ALS demonstrate cognitive
202 impairment reminiscent of FTLD, while ~1/3 of those with FTLD show motor neuron disease that is
203 indistinguishable from ALS (3, 45). These observations, as well as shared genetics underlying both
204 ALS and FTD, testify to the close overlap between ALS and FTLD with TDP43 pathology (FTLD-TDP)
205 (3, 45). Therefore, to determine if NLK dysregulation may be involved in ALS/FTLD-TDP disease
206 pathogenesis, we initially investigated *NLK* expression in *GRN* knockout mature brain organoids
207 (mbOrgs), an FTLD-TDP model that recapitulates key pathological features of disease, including
208 TDP43 mislocalization, phosphorylated TDP43, and characteristic missplicing of TDP43 substrate
209 RNAs (46). Neurogenin-2 inducible cortical neurons (iNeurons) and mature cortical astrocytes
210 (iAstrocytes) derived from isogenic wild-type (WT) or GRN-/- iPSCs were combined in fixed ratios to
211 form mbOrgs (Figure 7A). RNA-seq revealed significantly elevated normalized counts of *NLK* in
212 GRN-/- mbOrgs compared to WT controls (Figure 7B), a finding that was also confirmed by
213 quantitative RT-PCR (qRT-PCR) (Figure 7C).

214 To further explore the link between NLK changes and TDP43 pathology, we turned to a unique
215 dataset generated by Liu et al. in which neuronal nuclei were sorted from frontal cortices of FTLD-

216 TDP patients into two populations — those with and without nuclear TDP43 – prior to RNA
217 sequencing (RNA-seq) (30). Reanalysis of these data demonstrated a significant upregulation of
218 *NLK* mRNA in nuclei lacking TDP43 (Figure 7D). Using dual-immunohistochemistry, we confirmed
219 that spinal neurons from ALS spinal cord sections with TDP43 pathology (nuclear loss of TDP43
220 with cytosolic inclusions) exhibited more intense staining for NLK in comparison to unaffected
221 neurons present in the same section (Figure 7E and S5C). Dual staining for NLK and TDP43 was
222 also performed in sections from four control patients without spinal pathology (Figure S5D5),
223 showing no clear differences in NLK abundance. These results demonstrate a clear relationship
224 between elevated NLK, at both the mRNA and protein levels, and TDP43 mislocalization in FTLD-
225 TDP and ALS.

226 Together, these data show that NLK is upregulated in human patients and in disease models
227 featuring TDP43 pathology, in accord with our data demonstrating TDP43 mislocalization upon NLK
228 overexpression.

229

230 **NLK reduction improves survival in iPSC-derived neuron models of ALS**

231 Given the detrimental effects of NLK overexpression on nucleocytoplasmic transport (Figures 1-6)
232 and neuron survival (Figure 6), and the elevated *NLK* mRNA and protein observed in patients and
233 disease models (Figure 7A-E), we asked whether targeting *NLK* could ameliorate disease
234 phenotypes in ALS/FTLD-TDP models. First, we examined the survival of iPSC-derived neurons
235 carrying *C9ORF72* expansions, the most prevalent mutation underlying familial ALS and FTLD-TDP
236 in Europe and North America (47, 48). Non-disease and *C9ORF72* mutant neurons were
237 transduced with virus encoding non-targeting or *NLK* shRNA, resulting in a ~50% reduction in NLK
238 RNA levels compared to non-targeting shRNA (Figure 7F). Individual neurons were followed by

239 automated microscopy for 10 days, as before (Figure 7G), and differences in survival assessed via
240 Cox proportional hazards analysis. Three separate lines of *C9ORF72* mutant neurons exhibited
241 significantly higher cumulative risks of death compared to unrelated non-disease neurons (Figure
242 7H and S6A-C). Transduction with *NLK* shRNA significantly reduced the cumulative risk of death in
243 all three lines of *C9ORF72* neurons (HR= 0.403, p= 7.71e-50). To examine if NLK reduction is
244 neuroprotective outside of *C9ORF72* mutations, we utilized an isogenic pair of *TARDBP* mutant
245 iPSC-derived neurons that were created by CRISPR/Cas9 genome engineering (49). In comparison
246 to isogenic controls ("WT"), *TARDBP* mutant (M337V) neurons transduced with lentivirus
247 expressing non-targeting shRNA exhibited a significantly higher cumulative risk of death (Figure 7I).
248 As with *C9ORF72* mutant neurons, however, transduction with *NLK* shRNA-expressing virus
249 significantly extended the survival of M337V neurons (HR = 0.227, p= 0.0013). Collectively, these
250 data imply that *NLK* overexpression is toxic, while *NLK* reduction promotes neuronal survival in
251 models of ALS and FTLD-TDP.

252

253 **Discussion**

254 Our findings indicate that NLK overexpression disrupts the nuclear import and localization of
255 TDP43 and related RNA-binding proteins, including FUS and HNRNPA2B1, in a kinase-dependent
256 manner. These effects correlate with the mislocalization of the RanBP2-RanGAP1 complex and
257 collapse of the Ran gradient, both of which are crucial for functional nucleocytoplasmic transport.
258 As expected based on these observations, NLK dose-dependently increased the risk of death in
259 primary rodent neurons. Notably, we uncovered elevated NLK expression selectively in neurons
260 with TDP-43 pathology both at the RNA level (in FTLD-TDP frontal cortex) and at the protein level (in
261 ALS spinal cord). NLK was also upregulated in a brain organoid model of FTLD-TDP, while reducing

262 NLK in human iPSC-derived neurons carrying disease-associated mutations prolonged survival.
263 These results suggest that NLK may contribute to the pathology of ALS-FTLD-TDP by impairing
264 nucleocytoplasmic transport and promoting neurotoxicity. Targeting NLK protein levels or kinase
265 activity could thus represent a novel therapeutic approach for ALS, FTLD-TDP and other TDP43
266 proteinopathies.

267 Disruption of the Ran gradient, mislocalization of nuclear pore components, and disturbance of
268 nuclear pore architecture — all of which we observed upon NLK overexpression — have likewise
269 been described in ALS/FTLD-TDP samples and disease models (9-11, 50). There is no predicted
270 NLK phosphorylation site within TDP43 itself; rather, we suspect that NLK may interfere with the
271 nucleocytoplasmic transport of several RNA binding proteins and other factors by acting on
272 integral components of the nuclear pore. We and others noted a direct interaction between NLK
273 and the RanGAP1-RanBP2 complex ((30); see Figure 4), which is critical for maintaining the Ran
274 gradient and nuclear import/export (51). NLK overexpression prevented RanGAP1 sumoylation
275 (Figure 4A) and reduced the amount of RanGAP1 in complex with RanBP2 (Figure 4C). In the
276 absence of sumoylation, RanGAP1 is unable to bind RanBP2 or localize to the nuclear envelope
277 (Figure 4C, (31-33). One possibility is that NLK directly phosphorylates RanGAP1, inhibiting its GAP
278 activity (50) as well as its sumoylation, thereby disrupting its interaction with RanBP2 at the nuclear
279 pore complex. Alternatively, NLK may negatively regulate Ubc9, a SUMO E3 ligase required for
280 recruitment of RanGAP1 to the RanBP2 complex. None of these possibilities are mutually
281 exclusive; NLK may impact nucleocytoplasmic transport through more than one overlapping
282 mechanism.

283 At baseline, NLK is highly expressed in the CNS, and its expression is unregulated by oxidative and
284 osmotic stress (52, 53), conditions associated with the cytosolic accumulation of TDP43 and other,
285 predominantly nuclear, RNA binding proteins. NLK interacts with several proteins associated with

286 neurodegenerative diseases, including poly-Q expanded androgen receptor in spinobulbar
287 muscular atrophy (SBMA) and ataxin-1 in spinocerebellar ataxia 1 (SCA1) (16, 17); accumulations
288 of these proteins may also contribute to changes in NLK expression and/or activity. Although
289 previous studies have failed to detect NLK upregulation in disease, in most cases these
290 investigations are limited to evaluation of NLK levels (RNA or protein) in bulk tissue. In contrast, our
291 work revealed NLK upregulation solely within affected neurons displaying TDP43 pathology, in
292 association with evidence of disrupted nucleocytoplasmic trafficking in the same cells, suggesting
293 that NLK expression changes are restricted to cells with TDP43 redistribution. Outside of changes
294 in expression, NLK may also be inappropriately activated in disease via diverse stimuli.
295 Proinflammatory factors such as transforming growth factor ß (TGFß), interleukin-6 (IL6) and Wnt
296 all activate NLK through MAPK-dependent signaling (54). Notably, TGF-ß is upregulated in ALS (55),
297 and aberrant Wnt signaling is associated with TDP43 mislocalization in cellular and animal models
298 (56).

299 NLK is an essential kinase — homozygous *Nlk* deletion results in death *in utero* or postnatally,
300 depending on the mouse strain (57, 58). Conditional *Nlk* knockout in adult animals is well-
301 tolerated, however (59), and *Nlk* haploinsufficiency (*Nlk*+/-) is protective in several
302 neurodegenerative disease models, including TDP43-overexpressing mice (15-18). Similarly, partial
303 *NLK* knockdown in our investigations was associated with extended survival in *C9ORF72* and
304 *TARDBP* mutant human iPSC-derived neurons and was safe in control neurons. These data indicate
305 that even modest reductions in *NLK* may be sufficient for mitigating neurodegeneration in ALS and
306 FTLD-TDP.

307 Although prior interaction studies highlighted several potential partners for NLK, its substrates in
308 neurons and phosphorylation sites within these substrates remain largely unexplored. RanBP2 and
309 RanGAP1 are two potential targets for NLK with clear connections to nucleocytoplasmic transport,

310 but NLK is also likely to act on distinct substrates and disease-related pathways, including the
311 integrated stress response and autophagy (15). One advantage of therapeutic strategies that act on
312 upstream signaling factors such as NLK is the capacity to influence several neuroprotective
313 mechanisms simultaneously. Nevertheless, not all downstream events are likely to be
314 beneficial(18), emphasizing the need for further investigations into NLK targets and the impact of
315 NLK-mediated phosphorylation on their function and contribution to disease.

316

317

318 **Methods**

319 **Sex as a biologic variable**

320 Our study examined tissue from both male and female patients, and similar findings are reported
321 for both sexes.

322

323 **HEK293 cell culture and transfection**

324 Human embryonic kidney (HEK) 293T were cultured in DMEM (Gibco, 11995065) supplemented
325 with 10% FBS (Gibco, ILT10082147) at 37°C in 5% CO2. Cells were transfected with Lipofectamine
326 2000 (Invitrogen, 11668027) according to the manufacturer's instructions. For experiments with
327 YFP-NLS reporters, the lipofectamine solution was divided toto ensure there would be both cells
328 co-transfected with NLK and reporter as well as cells transfected with the reporter alone. Of the
329 lipofectamine solution, 75% contained two plasmids (NLK and reporter) while the remaining 25%
330 contained reporter alone. The lipofectamine solution was then combined and briefly mixed before
331 adding directly to cells. After 24 hours, transfected cells were split in media containing poly D-

332 lysine (1:500, cat Millipore A-008-E) onto coverslips coated with laminin (1:100, Sigma L2020-
333 1MG). Cells were cultured an additional 24 hours then immunocytochemistry was performed as
334 detailed below.

335

336 **Primary neuron cell culture and transfection**

337 Cortices from embryonic day (E)19-20 Long-Evans rat embryos were dissected and disassociated,
338 and primary neurons were plated at a density of $6x10^5$ cells/mL in 96-well plates or in 24 well plate
339 on coverslips. At *in vitro* day (DIV) 4, neurons were transfected using Lipofectamine 2000 as
340 previously described (49, 60). For experiments with the YFP-NLS reporter, the transfection mix was
341 split as described above for HEK cells. Following transfection, cells were placed in Neurobasal
342 Complete Media (Neurobasal (Gibco 21103-049), 1x B27 Supplement (Gibco, 17504-044), 1x
343 Glutamax, 100 units/mL Pen Strep). Cells were fixed for immunocytochemistry 48 hours after
344 transfection.

345

346

347 **iPSC maintenance and differentiation**

348 Creating Neural Progenitors: iPSCs were dissociated using Accutase, counted, and plated at
349 32,000 cells/mL in E8 media with ROCK inhibitor. Differentiation was then induced with
350 doxycycline for 48 hours (2 µg/mL; Sigma, #D3447). Differentiating neural progenitors (NP) were
351 dissociated using Accutase after two days of doxycycline induction and frozen for future
352 experiments.

353 Differentiating Neural Progenitors: Previously frozen neural progenitors were thawed in E8 media
354 with ROCK inhibitor and incubated for 24 hours. Subsequently, the media was changed to N2
355 media containing 1x N2 Supplement (Gibco, #17502-048), 1x NEAA Supplement (Gibco, #11140-
356 050), 10 ng/mL BDNF (Peprotech, #450-02), 10 ng/mL NT3 (Peprotech, #450-03), 0.2 µg/mL
357 Laminin (Sigma, #L2020), and 2 µg/mL doxycycline (Sigma, #D3447). On Day 2, the media was
358 replaced with transition media (1:1 full E8 media and DMEM/F12 (Gibco, #11320-033)). On Day 3,
359 the media was switched to B27 media, prepared with 1x B27 Supplement (Gibco, #17504-044), 1x
360 Glutamax Supplement (Gibco, #35050-061), 10 ng/mL BDNF, 10 ng/mL NT3, 0.2 µg/mL Laminin, 1x
361 CultureOne (Gibco, #A33202-01), and Neurobasal-A (Gibco, #12349-015). On Day 6, cells were
362 transduced with the virus (University of Michigan Vector Core) and maintained in the same media
363 for the remainder of the experiment.

364

365 **iPSC cell lines**

366 The cell lines 1021 and 793 (controls) and 883 and 321 (C9ORF) were generated and characterized
367 as previously described (7).. The CS52i and corrected cell lines were obtained from Cedars Sinai.
368 See table below for additional details.

	ID	Onset age	Biopsy age	Gender	Onset	Notes
C9orf72-fALS	C9b (883)	49	51	M	Lumbar	C9orf72 mutation +
	C9a (312)	52	54	M	Lumbar	C9orf72 mutation +
	C9c	46	47	M	Lumbar	C9orf72 mutation +

	(CS52)					
TDP43-fALS	TDP43 (M337V)		54	F		M337V and C-terminal Dendra2 inserted into ND1 (1021) by CRISPR/Cas9
	TDP43 (WT)		54	F		C-terminal Dendra2 inserted intoND1 (1021) by CRISPR/Cas9
Control	ND1 (1021)		54	F		Healthy
	ND2 (746)		58	M		Healthy
	C9c-corrected	46	47	M	Lumbar	C9orf72 mutation removed from CS52i by CRISPR/Cas9

369

370 **mbOrg generation**

371 Isogenic human iPSC line WTC11 (GRN+/+ and GRN−/−) were generated by Dr. Bruce R. Conklin, as
372 previously described (61). iPSCs were cultured and maintained in StemMACS™ iPS-Brew XF
373 (Miltenyi Biotec, 130-104-368) media on 6-well cell culture plates (GenClone, 25-105MP) coated
374 with Vitronectin (Gibco, A14700) in DPBS. iPSCs were dissociated and passaged using EDTA
375 (Invitrogen, AM9260G) in DPBS.

376 iA and iN were differentiated separately, plated in a 1:1 ratio, and aged for 4 weeks as previously
377 described (46). For iN differentiation, iPSCs were transduced with NGN2-expressing lentivirus
378 constructs and a previously published protocol was followed for differentiation (61). Briefly, iPSCs
379 are expanded, dissociated, and replated on Matrigel-coated plates. Cells are grown in specialized
380 iNeuron induction media (DMEM-F12 + Glutamax; Gibco, 10565-018), N-2 supplement (Gibco,
381 17502-048), MEM-NEAA (Gibco, 11140-050) containing doxycycline (Sigma, D3072) for 72 h, with

382 media changed every 24 h. Cells are then dissociated using Accutase and plated together with iA.
383 Cortical-like iA are generated as previously described (62). Human induced pluripotent stem cells
384 (GRN+/+ and GRN-/-) were grown on vitronectin coated tissue culture plates using StemMACS™
385 iPS-Brew XF (Miltenyi Biotec, 130-104-368) media. On day 0 of differentiation, iPSCs are
386 dissociated into small aggregates and transferred in neurosphere induction medium (NSIM)
387 (DMEM-F12/Neurobasal-A at 1:1) plus SMAD inhibitors SB431542 and DMH1. On day 7, spheroids
388 are transferred to Matrigel-coated tissue culture plates with NIM. On day 14, rosette clusters were
389 mechanically removed and transferred to tissue culture flasks with NIM plus FGFb (Peprotech,
390 100-18B). Media was changed every 72 hours. On day 20, spheroids were triturated into a single
391 cell suspension and transferred to a new untreated cell culture flask with astrocyte media (ASM)
392 [(DMEM-F12 (Gibco, 10565-018), N2 Supplement (Gibco, 17502-048), B27 -Vit.A Supplement
393 (Gibco, 12587-010), Heparin (Stemcell Tech, 07980)) plus Y27632 (Tocris, 1254)]. From Day 28 to
394 180, spheroid aggregates were maintained in suspension with ASM plus EGF and FGFb (Peprotech,
395 100-15 & 100-18B) with media changes every 4-5 days. Spheroid aggregates were triturated every
396 7-10 days and transferred to new untreated tissue culture flasks. Spheroids are triturated every 7–
397 10 days and transferred to new tissue culture flasks. In order to generate mbOrgs, iN and iA are
398 plated together at a 1:1 ratio on Matrigel-coated 24-well plates at a collective density of ~1x106
399 cells/well. Cells are maintained in BrainPhys Complete medium with a 50% medium change every
400 72 h. mbOrgs will be created on 384-microwell plates as described previously (46), resulting in
401 mbOrgs that are highly uniform in size (~500 m) after brief spin-down and 1–2 days of subsequent
402 culture. These 3D co-cultures were aged for 4 weeks.

403

404 **Longitudinal microscopy**

405 At in vitro day (DIV) 4, neurons were transfected with 100ng of a control fluorescent plasmid to
406 mark cell bodies and 100ng of an experimental construct using Lipofectamine 2000 as previously
407 described (43, 49, 62). Neurons were imaged as described previously (43, 49, 60, 63) using a Nikon
408 Eclipse Ti inverted microscope with PerfectFocus3a 20X objective lens and either an Andor iXon3
409 897 EMCCD camera or Andor Zyla 4.2 (+)sCMOS camera. A Lambda CL Xenon lamp (Sutter) with 5
410 mm liquid light guide (Sutter)was used to illuminate samples, and custom scripts written in
411 Beanshell for use in micromanager controlled all stage movements, shutters, and filters. For
412 automated analyses of primary neuron survival, custom ImageJ/FIJI macros and Python scripts
413 were used to identify neurons and draw cellular regions of interest (ROIs) based upon size,
414 morphology, and fluorescence intensity. Custom Python scripts were used to track ROIs over time,
415 and cell death marked a set of criteria that include rounding of the soma, loss of fluorescence and
416 degeneration of neuritic processes (63, 64). For iNeuron survival, brightfield and fluorescent
417 images for survival experiments started on Day 14 and continued for 10 days. For manual analysis
418 of iNeuron survival, image time-series were processed by flat-field correction and image
419 registration, followed by programmatic de identification for blinded analysis. Time-series images
420 were uploaded to a browser-based server where a trained user manually counted survival using the
421 point tracking mode. GFP-positive cells were identified at T1, and cell fate was tracked in brightfield
422 images, where neuron death (uncensored event) was recorded at the appropriate time point. Living
423 neurons at the final time point were considered right-censored. Cox proportional hazards model
424 was applied to the datasets, stratifying by biological replicates, and the corresponding hazard plots
425 were generated in R.

426

427 **Immunocytochemistry**

428 Cells were fixed with 4% paraformaldehyde (PFA; Sigma, P6148) for 10m, rinsed with PBS, and
429 permeabilized with 0.1% Triton X-100 (Bio-rad, 161-0407) for 10m. Cells were then blocked in 3%
430 bovine serum albumin (BSA; Fisher, BP9703-100) in PBS at RT for 1h before incubation O/N at 4°C
431 in primary antibody diluted in 3% BSA (See table for additional details). Cells were then washed 3
432 times in PBS and incubated at RT with secondary antibodies diluted 1:250 in 3% BSA for 1h.
433 Following 3 washes in PBS containing 1:10,000 Hoechst 33258 dye (Invitrogen, H3569), cells were
434 mounted on Superfrost Plus Microscope Slides (Fisher, 1255015) with Prolong Gold Antifade
435 Mounting Reagent (Fisher, P10144) and imaged as described below. Images were analyzed by
436 collecting measurements within cellular regions of interest using custom ImageJ/FIJI macros.
437 Graphs were made using R.

438

439 **Fluorescence in situ hybridization**

440 Cells were fixed with 4% paraformaldehyde (Cat #) for 10 m, rinsed with PBS and permeabilized
441 with 0.1% Triton X-100 (Bio-rad, 161-0407) for 10m. Cells were then washed with 2X SSC (2 x 5 m)
442 and incubated in hybridization buffer for 2 hours at 37 degrees (8.75% dextran, 1.75X SSC, 17.5%
443 formamide, 0.5 ug/ul yeast tRNA, 10 mmol RVC, 0.1% BSA, 0.002 ug/ul Cy3-oligo (dT) 30 probe).
444 Cells were then washed with successive SSC rinses (4X SSC 15 m, 2X SSC 15 m, 2X SSC 15m).
445 Then immunocytochemistry was performed as above, beginning with blocking in 3% BSA. All
446 solutions prior to hybridization were DEPC treated.

447

448 **Immunohistochemistry**

449 Duplex immunohistochemistry was performed on a Ventana Discovery Ultra stainer (Indianapolis,
450 IN). Slides were dewaxed, rehydrated and subjected to heat induced epitope retrieval on board the
451 stainer. Slides were then subjected to sequential incubation with NLK (Rabbit polyclonal antibody,
452 AbCam, Cambridge, MA, Ab26050, 1:250, 32 minutes) and polymer goat anti-rabbit IgG conjugated
453 to HRP (Ventana) and developed with Discovery Green chromogen (Ventana). After an additional
454 round of heat induced epitope retrieval to remove the NLK primary antibody-secondary antibody
455 complex, the slides were stained with TDP43 (Rabbit polyclonal antibody, Proteintech, Rosemont,
456 IL, 10782-2-AP, 1:2000, 20 minutes), polymer goat anti-rabbit IgG conjugated to HRP and
457 developed with Discovery Brown chromogen (Ventana). Slides were then countered stained with
458 hematoxylin and coverslipped.

459

460 **RNA isolation for bulk RNAseq and RT-PCR**

461 RNA extraction was performed using the Trizol/phenol-Chloroform method (Sigma, T9424) as
462 previously described (62) and according to manufacturer specifications. Each sample contained
463 ~60 mbOrgs, totaling ~3 x10^6 of cells per sample. The extracted RNA was used as a template for the
464 synthesis of complementary DNA (cDNA) through reverse transcription, using iScript™ cDNA
465 Synthesis Kit (Bio-Rad Cat#1708891) according to the manufacturer's protocol.

466

467 **Quantitative PCR**

468 cDNA samples were treated for genomic DNA contamination using DNA-*free*™ DNA Removal Kit
469 (Invitrogen Cat#AM1906) per manufacturer's instructions. The cDNA was then diluted to a
470 concentration of 5 ng/µl and 4 µl of each sample (total of 20 ng) were aliquoted in a MicroAmp™
471 Optical 96-Well Reaction Plate (Thermo Scientific Cat#N8010560) in technical duplicates. Samples
472 were processed using 2X SYBR Green qPCR Master Mix Assay and quantitative PCR was run on

473 QuantStudio 6 Real-Time PCR system following manufacturer's instructions. Data analysis was
474 carried out applying the Pfaffl mathematical model for relative transcript quantification (65) using
475 GAPDH as a housekeeping gene.
476

477 **RNA Sequencing**

478 RNA sequencing and analysis of RNA integrity was analyzed on an Agilent 2100 Bioanalyzer using
479 RNA 6000 Nano kit (Agilent, 5067-1511). Only samples with an RNA integrity number (RIN) ≥ 9.4
480 were used to perform bulk RNA sequencing. Nugen Universal Plus (Tecan) was used as a library kit
481 and libraries were sequenced on a SP300 flow cell of the Illumina NovaSeq 6000 machine with a
482 paired end 150 bp sequencing strategy (average depth 90 million reads/sample) at UCSF Genomics
483 Core Facility. Genome was aligned to Ensembl Human.GRCh38.103. Kallisto 0.46.01 was used to
484 generate transcript abundance files for each sample. Transcript counts files for each sample were
485 generated using txImport and transcript differential analysis was performed using DESeq2 v1.24.0.
486 A total of 6 samples were spread across two conditions.
487

488 **Confocal microscopy**

489 Confocal images were taken on a Nikon AXR NSPARC confocal system with a 60x NA1.42 Oil/DIS
490 PLan-Apochromat Lambda D objective with a working distance of 1.5 mm, and a 40x CFI
491 Apochromat LWD Lambda S objective with a working distance of 0.30 mm.

492

493 **Light microscopy**

494 Whole-slide images were generated by the University of Michigan Digital Pathology group within the
495 Department of Pathology using an Aperio AT2 scanner (Leica Biosystems) equipped with a 20x NA
496 0.75 Plan Apochromat objective. 40x scanning is achieved using a 2x optical magnification
497 changer. Resolution is 0.25 μm/pixel for 40x scans. Focus during the scan was maintained using a
498 triangulated focus map built from individual focus points determined in a separate step before
499 scanning was started. Proprietary software was used for image processing during the acquisition.
500 TIFs were taken of the entire ventral horn of all cases, then a pathologist selected each neuron,
501 manually drew an ROI, and annotated the TDP status (pathology or no pathology) using custom Fiji
502 scripts. Then deconvolution and analysis were performed using custom Fiji scripts.

503 High quality images for figures were acquired on an Olympus BX51 light microscope equipped with
504 a UPlanSApo100x oil objective with a numerical aperture of 1.40 and a working distance of 0.12
505 mm. Image deconvolution was performed using Fiji.

506

507 **Antibodies**:

	Vendor	Catalog #	Concentration for ICC
Flag	AbCam	ab1170	1:200
TDP43	R&D	MAB7778	1:200
TDP43	Proteintech	10782-2-AP	1:200
FUS	Sigma	HPA008784	1:200

HNRNPA2B1	Proteintech	14813-1-AP	1:100
MATR3	Abcam	ab281927	1:200
V5	Abcam	ab53418	1:200
KPNA2	Proteintech	10819-1-AP	1:200
KPNB1	Abcam	AB2811	1:200
Ran	BD Transduction labs	610340	1:400
RanGAP	Abcam	AB92360	1:200
RanBP2	Abcam	AB64276	1:200
Mab414	Abcam	AB24609	1:200
NXF1	Abcam	AB129160	1:200
SC-35	Sigma	S4045-.2ML	1:200
SFPQ	Proteintech	15585-1-AP	1:200
Nucleophosmin	Millipore	MABE937	1:200

508

509 **Plasmids**

Plasmid	Source
FLAG-NLK-WT	Gift from T. Ishitani (66)
FLAG-NLK KN (K155M)	Gift from T. Ishitani (66)
EYFP2-SV40NLS-NES	Gift from Yuh Min Chook (67)
EYFP2-SV40NLS	This paper
EYFP2-TDPNLS	This paper
EYFP2-FUSNLS	This paper
EYFP-MATR3NLS	This paper
pGW1-TDP43(2F/L)-EGFP	Flores et al 2019 (36)
FUGW-SNAP-FLAG	This paper
FUGW-SNAP-FLAG-NLK	This paper

510

511 FLAG-NLK-WT and FLAG-NLK KN were a gift from T Ishitani . SNAP-FLAG and SNAP-FLAG NLK were
512 synthesized and subcloned into FUGW. All YFP reporter plasmids were derived from EYFP2-
513 SV40NLS-NES, a kind gift from Yuh Min Chook (67). Site-directed mutagenesis was used to add a
514 stop codon after the SV40NLS. The NLS of TDP43 (residues 82-98) and FUS (residues 495-526)
515 were PCR amplified using primers below, digested with XbaI and BglII, and cloned into the
516 corresponding sites in EYFP2-SV40NLS-NES. The NLS of MATR3 (residues 583-602) was purchased
517 as a Geneblock from Integrated DNA Technologies (IDT), and then digested with XbaI and BglII, and

518 cloned into the corresponding sites in EYFP2-SV40NLS-NES. All plasmids were verified by Sanger

519 sequencing.

520

521 **Primers**

Amplify TDP43 NLS	For: ctcagatctcgaAAAAGAAAAATGGAT Rev: ttatctagagatTCTTTTCACTTTCAC
Amplify FUS NLS	For: tcagatctCGAGGGGGCCGGGGT Rev: tatctagaATACGGCCTCTCCCT
Mutagenesis: introduce stop codon into EYFP2-SV40NLS-NES	For: ctcgaccaaaaaagaagagaaaggtataagctttagccttgaaa Rev: tttcaaggctaaagcttatacctttctcttctttttggtcgag
qPCR NLK	For: GGGTCCTCATAAACAGCCATC Rev: AGACCAACATCCTGCAAAGG
qPCR GAPDH	For: GGG GTC ATT GAT GGC AAC AAT A Rev: ATG GGC AAG GTG AAG GTC G

522

523 **Data analysis and statistics**

524 Statistical information, including mean and statistical significance values is indicated in the figures
525 or figure legends. At least three biological replicates were used per experiment. For analysis of
526 immunocytochemistry images, ROIs for nucleus and cytoplasm were either generated using CVAT
527 (68) or manually drawn in ImageJ. Nuclear/cytoplasmic ratio was calculated and statistical
528 significance was determined with GraphPadP Prism 9 using the tests indicated in each figure. Data
529 were considered statistically significant at *P < 0.05, **P < 0.01, ***P < 0.001 and ****P < 0.0001.
530 Data from Liu et al. was analyzed with assistance from the TDP43 loss of function database (69);
531 DESeq2 *P*-values were calculated using Wald tests and corrected for multiple testing using the
532 Benjamini–Hochberg method. DEU events with *P*adj <0.05 were considered significantly changed.

533

534 **Study approval**

535 Skin samples for iPSC creation were collected and de- identified in collaboration with the Michigan
536 Institute for Clinical and Health Research (MICHR, UL1TR000433) through an institutional review
537 board (IRB)-approved protocol (HUM00028826).

538

539 **Data availability**

540 All correspondence regarding the materials and data presented in this paper should be addressed
541 to sbarmada@med.umich.edu.

542

543 **Author Contributions**

544 MB and SB designed the study. EP and MB designed experiments with SB. MB and EP collected
545 data for most experimental studies, analyzed the data, assembled the figures, and wrote the
546 manuscript. MB and EP performed immunocytochemistry. JM assisted with data collection and
547 analysis. MB performed survival assays in cultured rat neurons and iNeurons, wrote custom FIJI
548 scripts for quantitation of immunocytochemistry and dual IHC. EP made YFP reporter constructs,
549 supervised dual IHC (with the IHC core),and selected motor neurons for quantitation. LGG and MM
550 contributed to mbOrg concept, development, and data analysis. MK and SC cultured mbOrgs and
551 performed RNASeq and qPCR. EU contributed to original concept and development of mbOrgs,
552 and provided RNA-seq data from mbOrgs. XL isolated and cultured rat cortical neurons. EMHT
553 derived iPSC lines and developed protocols for their differentiation. JW developed original code for
554 neuron segmentation and image processing. SB provided resources, funding, and conceptual input
555 for experiments and supervised the research. All authors were involved throughout the research
556 process, agreed amongst themselves regarding roles and responsibilities, and contributed to the
557 review, editing, and approval of the manuscript.

558

559 **Acknowledgements**

560 This work was supported by: National Institutes of Health AWD012778 (EP), National Institutes of
561 Health (R01NS097542, R01NS113943 and 1R56NS128110-01 to SJB; R44NS124457 to MM;
562 P30AG072931 to the University of Michigan Brain Bank and Alzheimer's Disease Research
563 CenterNational Institute on Drug Abuse R44NS124457 (MDM and EMU), the family of Angela
564 Dobson and Lyndon Welch, the A. Alfred Taubman Medical Research Institute, the Danto Family,
565 Ann Arbor Active Against ALS, and the Robert Packard Center for ALS Research.

566 We thank all members of the Barmada laboratory for their advice and suggestions. We thank Dr.
567 Dafydd Thomas of the Rogel Cancer Center Tissue and Molecular Pathology Shared Resource
568 Laboratory at the University of Michigan (NIH P30 CA04659229). We thank the Michigan Institute for
569 Clinical and Health Research (MICHR, UL1TR000433), who collaborated to collect and de-identify
570 skin samples for iPSC creation. Finally, we thank the patients that donated tissue samples to make
571 this work possible.

572 Schematics were created in BioRender. Barmada, S. (2024) BioRender.com/z94b294

Figure 1

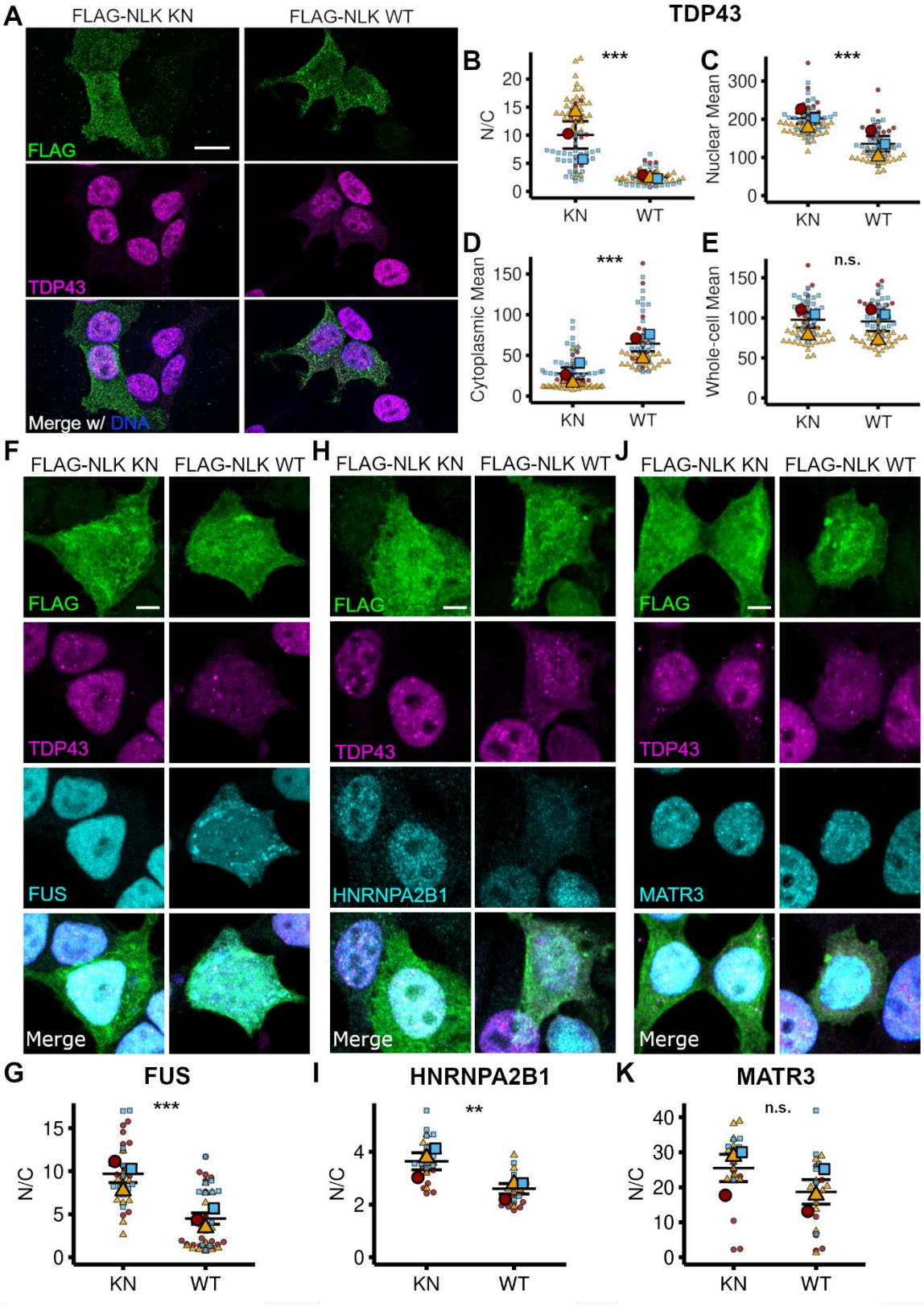
A
FLAG-NLK KN
FLAG-NLK WT
FLAG
TDP43
Merge w/ DNA
TDP43
B
N/C
***
KN
WT
C
Nuclear Mean
***
D
Cytoplasmic Mean
***
E
Whole-cell Mean
n.s.
F
FUS
Merge
H
HNRNPA2B1
J
MATR3
G
FUS
I
HNRNPA2B1
**
K
MATR3
n.s.

573

574

575 **Figure 1. Overexpression of NLK leads to cytoplasmic accumulation of TDP43 and ALS-FTD**
576 **relevant RNA-binding proteins.** (**A**) HEK cells were transfected with plasmids encoding either
577 FLAG-NLK KN (KN; kinase-negative) or FLAG-NLK WT (WT; wild-type) followed by
578 immunofluorescence using antibodies against FLAG and TDP4343 while DNA was stained with
579 Hoechst. Scale bar = 10μm. (**B**) Superplot of Nuclear-Cytoplasmic ratio (N/C) of TDP43 from
580 images in (A). Line = mean, error bar = standard error. *p<0.05, ** p<0.01, ***p<0.001. (unpaired T-
581 test with Welch's correction). (**C**) Superplot of TDP43 nuclear intensity in cells that overexpress KN
582 or WT NLK. Line = mean, error bar = standard error. (**D**) Superplot of TDP43 cytoplasmic intensity in
583 cells that overexpress KN or WT NLK. Line = mean, error bar = standard error. (**E**) Superplot
584 quantification of TDP43 whole-cell intensity in cells that overexpress KN or WT NLK. Line = mean,
585 error bar = standard error. (**F**) HEK cells were transfected with the indicated FLAG-NLK plasmids as
586 in (A) followed by immunofluorescence using antibodies against FLAG, TDP43, and FUS while DNA
587 was stained with Hoechst. Scale bar = 10μm (**G**) Superplot of FUS localization in cells that
588 overexpress KN or WT NLK. Line = mean, error bar = standard error. (**H**) HEK cells were transfected
589 with the indicated FLAG-NLK plasmids as in (A) followed by immunofluorescence using antibodies
590 against FLAG, TDP43, and HNRNPA2B1 while DNA was stained with Hoechst. Scale bar = 10μm. (**I**)
591 Superplot of HNRNPA2B1 localization in cells that overexpress KN or WT NLK. Line = mean, error
592 bar = standard error. (**J**) HEK cells were transfected with the indicated FLAG-NLK plasmids as in (A)
593 followed by immunofluorescence using antibodies against FLAG, TDP43, and MATR3 while DNA
594 was stained with Hoechst. Scale bar = 10μm. (**K**) HEK cells were transfected with the indicated
595 FLAG-NLK plasmids as in (A) followed by immunofluorescence using antibodies against FLAG and
596 MART3 while DNA was stained with Hoechst. Scale bar = 10μm. (**L**) Superplot of HNRNPA2B1
597 localization in cells that overexpress KN or WT NLK. Line = mean, error bar = standard error.

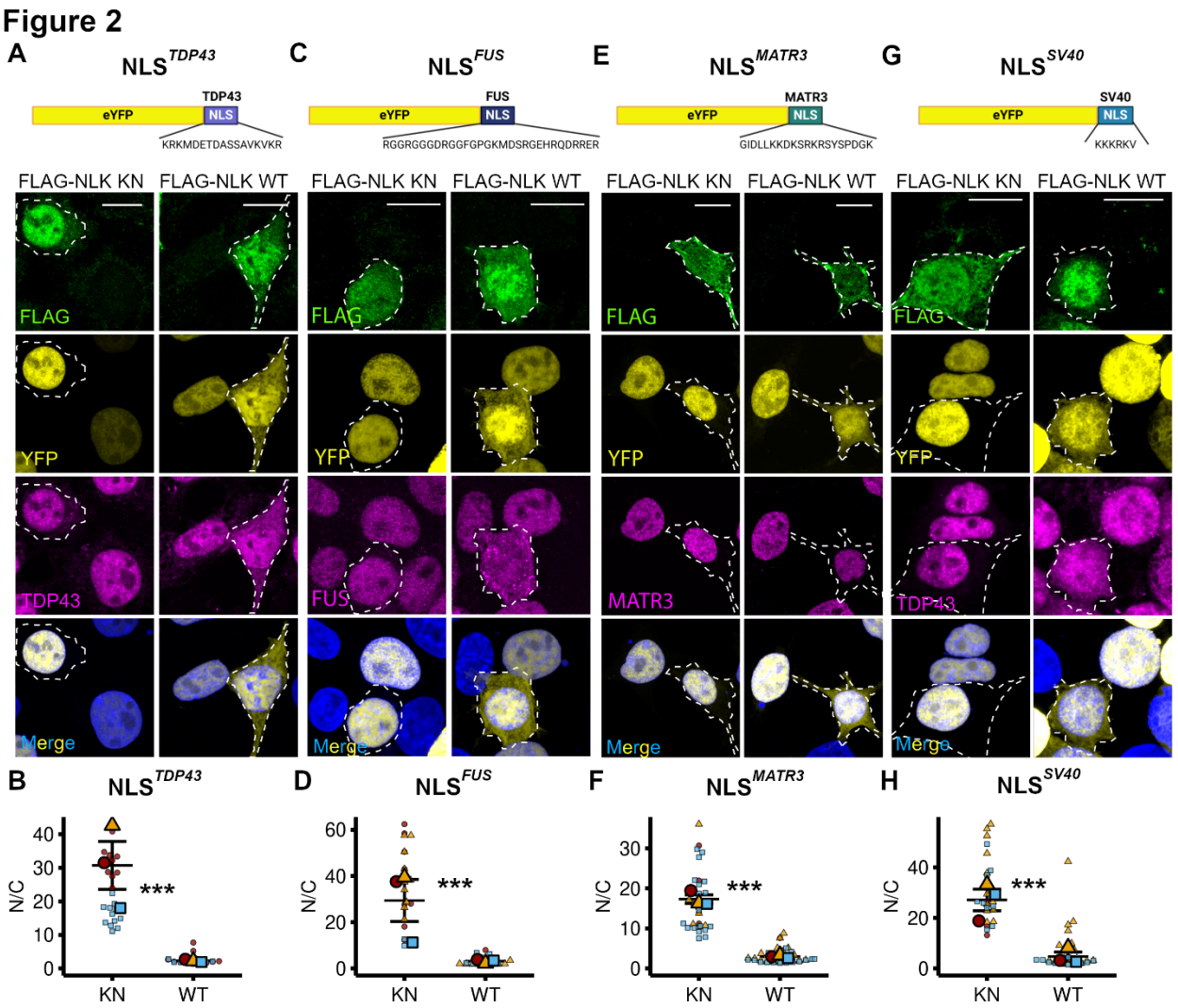

598

599

600 **Figure 2. NLK overexpression disrupts NLS dependent nuclear import.** (**A-D**) HEK cells were co-

601 transfected with plasmids encoding either FLAG-NLK KN or FLAG-NLK WT and either of the

602 following NLS-reporter eYFP-NLS^{TDP43} (A), eYFP-NLS^{FUS} (B), eYFP-NLS^{MATR3} (C), or eYFP-NLS^{SV40}.

603 Schematics created in BioRender. (D). Immunofluorescence was performed using antibodies

604 against FLAG and either TDP43, FUS, or Matrin-3 while DNA was stained with Hoechst. Scale bar 10

605 uM. (**E-H**) Superplot of NLS-reporter Nuclear-Cytoplasmic ratio (N/C) from images in A-D. Line =

mean, error bar= standard error. *** indicates p-value < 0.001 (unpaired t-test with Welch's correction).

Figure 3

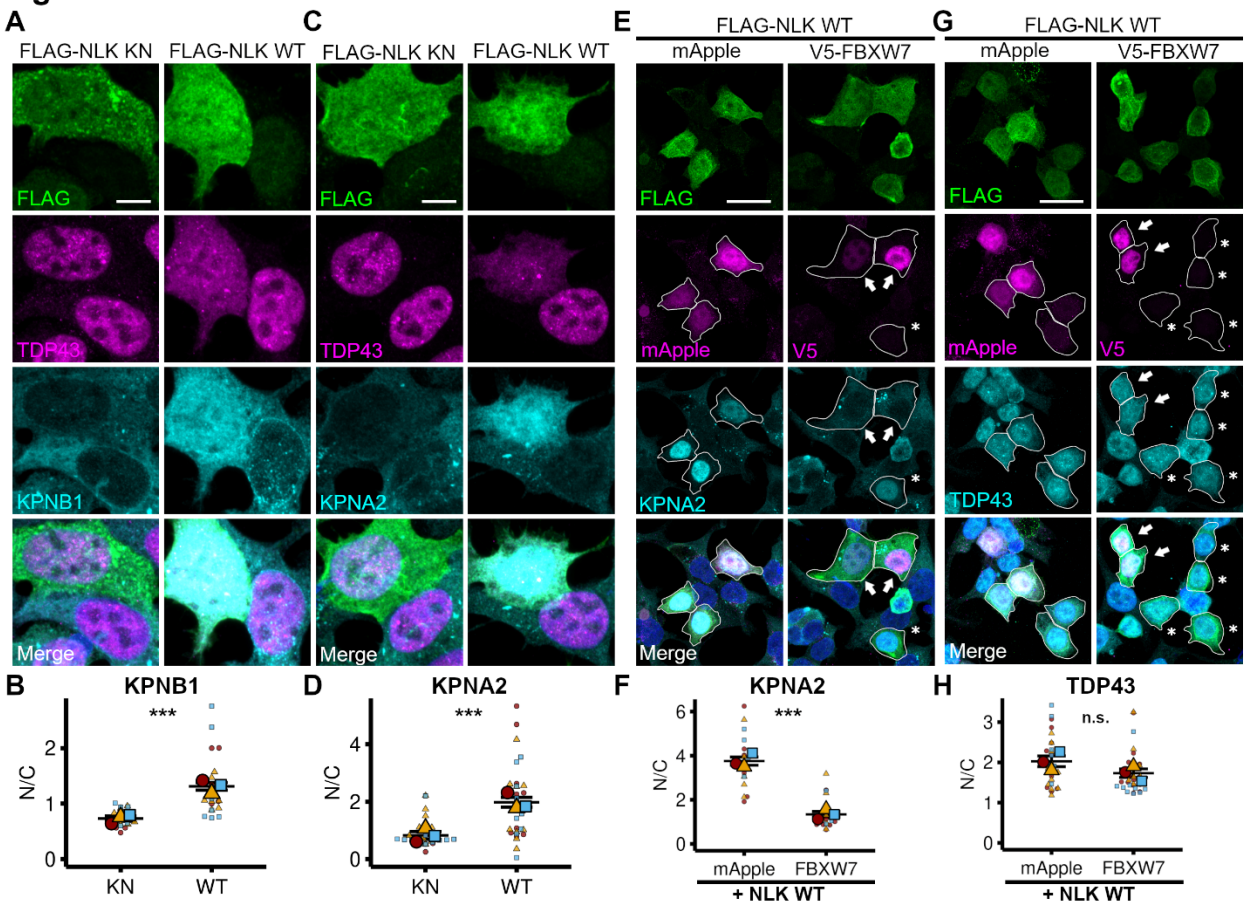

Figure 3. NLK-dependent mislocalization of TDP43 does not depend on nuclear accumulation of KPNA2 and KPNB1. (**A**) HEK cells were transfected with plasmids encoding either FLAG-NLK KN (KN; kinase-negative) or FLAG-NLK WT (WT; wild-type) followed by immunofluorescence using antibodies against FLAG, TDP43, and KPNA2 or KPNB1 while DNA was stained with Hoechst. Scale bar = 5μm. (**B**) Quantification of KPNA2 and KPNB1 localization in cells that overexpress NLK KN or WT. Line = mean, error bar = standard error. Statistical significance indicated as such in all sub-panels: n.s. = not significant, *p<0.05, ** p<0.01, ***p<0.001(unpaired t-test with Welch's correction).(**C**) HEK cells were co- transfected with plasmids encoding FLAG-NLK WT and either mApple (negative-control) or V5-FBXW7 followed by immunofluorescence using antibodies against

620 KPNA2, FLAG, and V5 while DNA was stained with Hoechst. Scale bar = 20μm. (**D**) Quantification of
621 KPNA2 localization in cells that overexpress FLAG-NLK WT and either mApple or V5-FBXW7. Line=
622 mean, error bar= standard error. *p<0.05, ** p<0.01, ***p<0.001 (unpaired t-test with Welch's
623 correction). (**E**) HEK cells were co-transfected with plasmids encoding FLAG-NLK WT and either
624 mApple or V5-FBXW7 followed by immunofluorescence using antibodies against TDP43, FLAG, and
625 V5 while DNA was stained with Hoechst. Scale bar = 20μm. (**F**) Quantification of TDP43 localization
626 in cells that overexpress FLAG-NLK WT and either mApple or V5-FBXW7. Line = mean, error bar=
627 standard error. *p<0.05, ** p<0.01, ***p<0.001 (unpaired t-test with Welch's correction). (G) HEK
628 cells were co-transfected as in E) followed by immunofluorescence using antibodies against
629 KPNA2, FLAG, and V5 while DNA was stained with Hoescht. Scale bar = 20 μm.(H) HEK cells were
630 co- transfected as in E) followed by immunofluorescence using antibodies against KPNA2, FLAG,
631 and V5 while DNA was stained with Hoechst. Scale bar = 20μm. (I) Quantification of KPNB1
632 localization in cells that overexpress NLK WT and either mApple orr V5-FBXW7. Line = mean, error
633 bar = standard error.

Figure 4

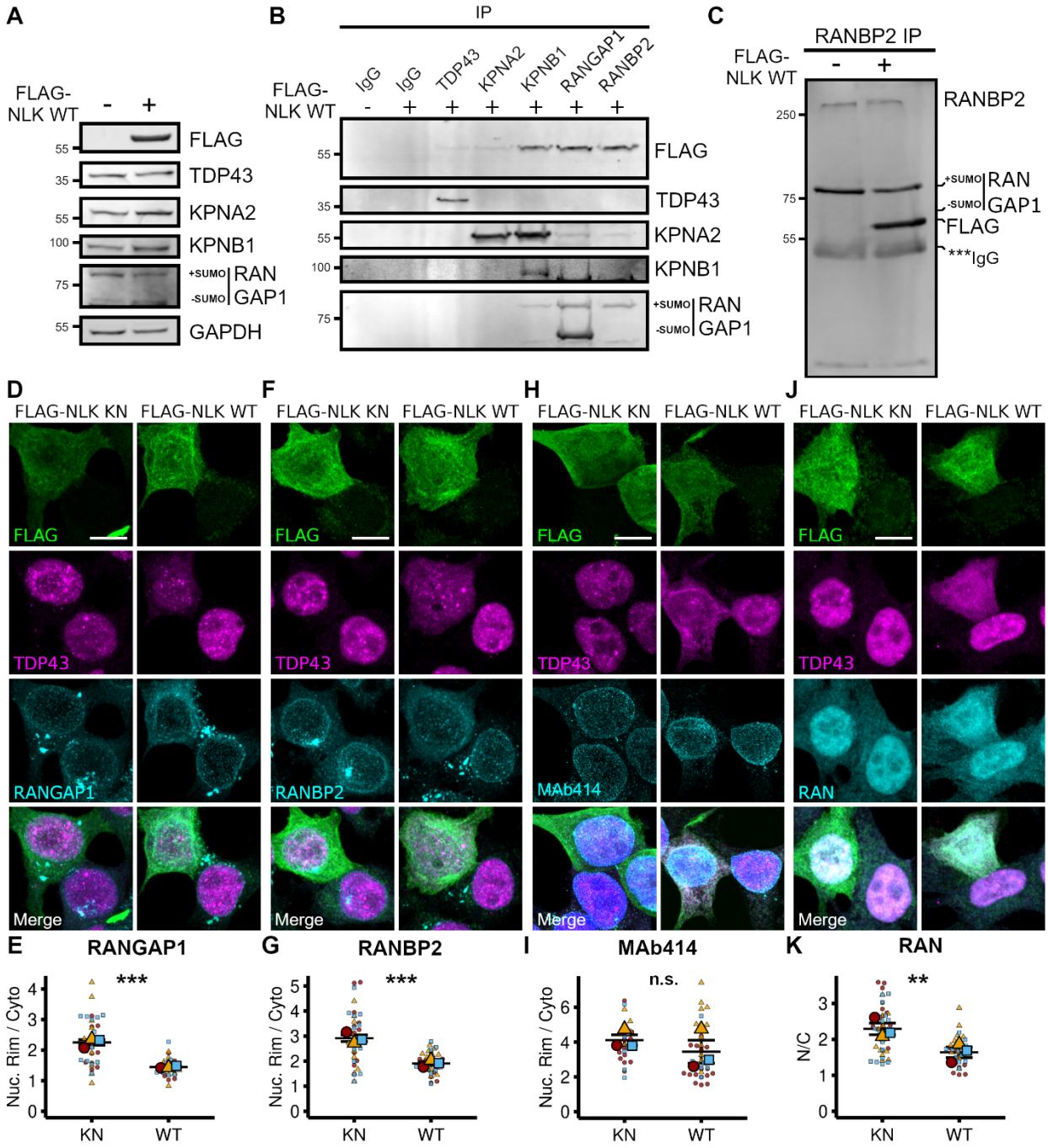

634

635

636 **Figure 4. NLK overexpression mislocalizes RanBP2-RanGAP1 and disrupts the Ran gradient.**

637 (**A**) Representative western blots from HEK cells transfected with either vector (-) or FLAG-NLK WT

638 (WT, +; wild-type). #'s to the left represent molecular weight in kDa. (**B**) Western blots after

639 immunoprecipitation (IP) using 1µg of the indicated antibodies in 1mg of lysates from (A). (**C**)
640 Western blots after RanBP2 co-IP from lysates in (A) were run on a 4-20% tris-glycine gel to
641 facilitate visualization of RanBP2 and validate NLK complex formation with RanBP2-RanGAP1-
642 SUMO. (**D**) HEK cells were transfected with plasmids encoding either FLAG-NLK KN (KN; kinase-
643 negative) or FLAG-NLK WT (WT; wild-type) followed by immunofluorescence using antibodies
644 against FLAG, TDP43, and either Ran, RanGAP1, RanBP2, or MAb414 (FG-nucleoporins) while DNA
645 was stained with Hoechst. Scale bar = 10µm. (**E**) Superplot of nuclear-cytoplasmic ratio (N/C) of
646 Ran. Line = mean, error bar= standard error. Statistical significance indicated as such in all sub-
647 panels: n.s. = not significant, *p<0.05, ** p<0.01, ***p<0.001. *p<0.05, ** p<0.01, ***p<0.001
648 (unpaired t-test with Welch's correction). (**F**) HEK cells were transfected as in (D) followed by
649 immunofluorescence using antibodies against FLAG, TDP43, and RANBP2 while DNA was stained
650 with Hoechst. Scale bar = 10µm. (**G**) Superplot of nuclear-rim-cytoplasm ratio (Nuc. Rim/Cyto) of
651 RANBP2. (**H**) HEK cells were transfected as in (D) followed by immunofluorescence using
652 antibodies against FLAG, TDP43, and MAB414 (FG-nucleoporins) while DNA was stained with
653 Hoechst. Scale bar = 10µm. (**I**) Superplot of nuclear-rim-cytoplasm ratio (Nuc. Rim/Cyto) of
654 MAB414. (**J**) HEK cells were transfected as in (D) followed by immunofluorescence using antibodies
655 against FLAG, TDP43, and RAN while DNA was stained with Hoechst. Scale bar = 10µm. (**K**)
656 Superplot quantification of nuclear-cytoplasm ratio (N/C) of RAN.

Figure 5

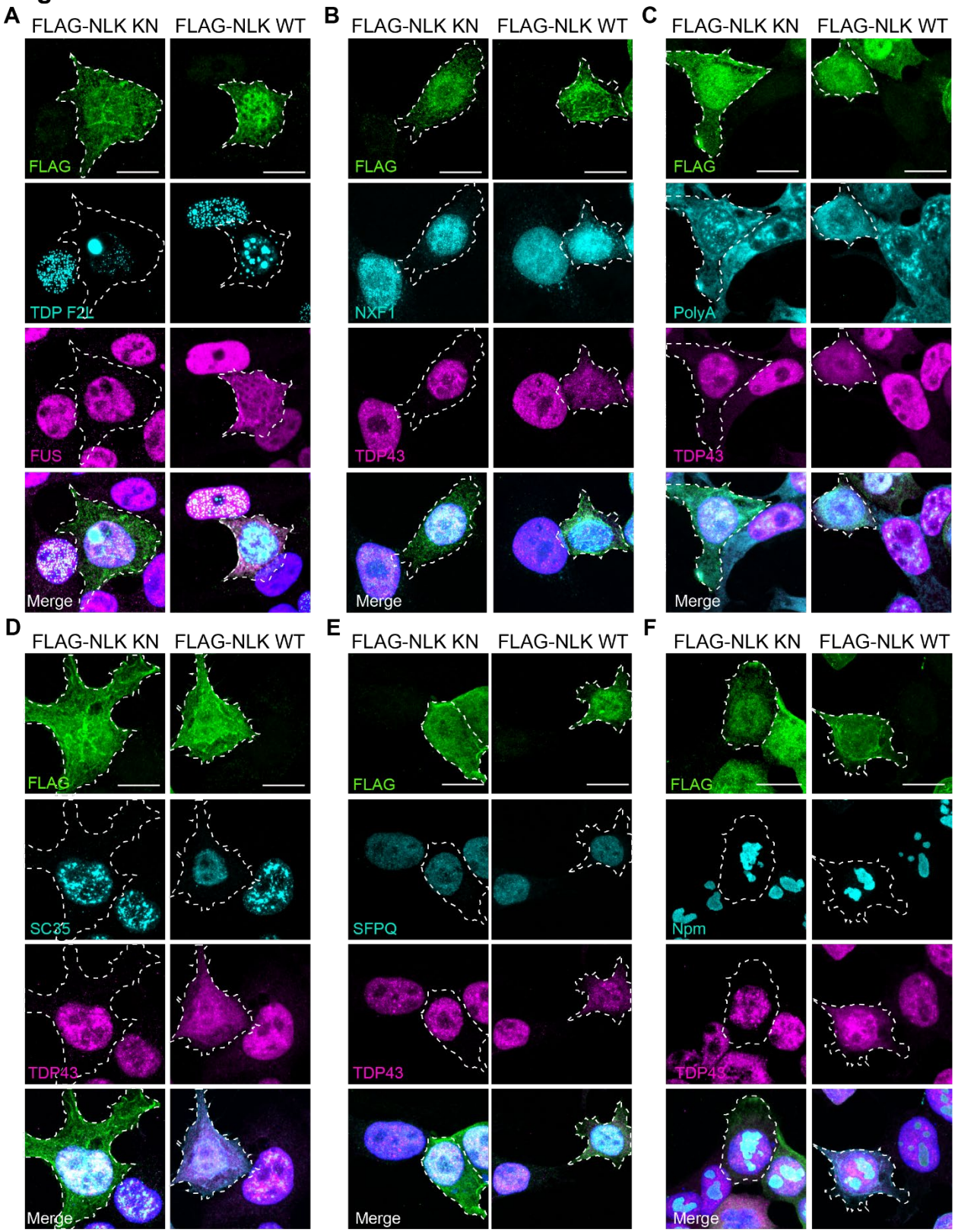

657

658

659 **Figure 5. NLK overexpression drives dissolution of nuclear speckles.** (**A**) HEK cells were co-
660 transfected with plasmids encoding either FLAG-NLK KN or FLAG-NLK WT and a GFP-tagged RNA-
661 binding mutant TDP43 (TDP43 F147/9L; F2L) followed by immunofluorescence using antibodies
662 against FLAG and FUS and direct visualization of tagged protein while DNA was stained with
663 Hoechst. Scale bar 10 μm. (**B**) HEK cells were transfected with plasmids encoding either FLAG-NLK
664 KN or FLAG-NLK WT followed by immunofluorescence using antibodies against FLAG, TDP43, and
665 NXF1. Scale bar 10 μm. (**C**) HEK cells were transfected with plasmids encoding either FLAG-NLK
666 KN or FLAG-NLK WT followed by polyA FISH and immunofluorescence for TDP43. Scale bar 10 μm.
667 (**D-F**) HEK cells were transfected with plasmids encoding either FLAG-NLK KN or FLAG-NLK WT
668 followed by immunofluorescence for TDP43 and markers of speckles (SC-35) (D), paraspeckles
669 (SFPQ) (E), or nucleolus (nucleophosmin, Npm) (F). Scale bar 10 μm.

Figure 6

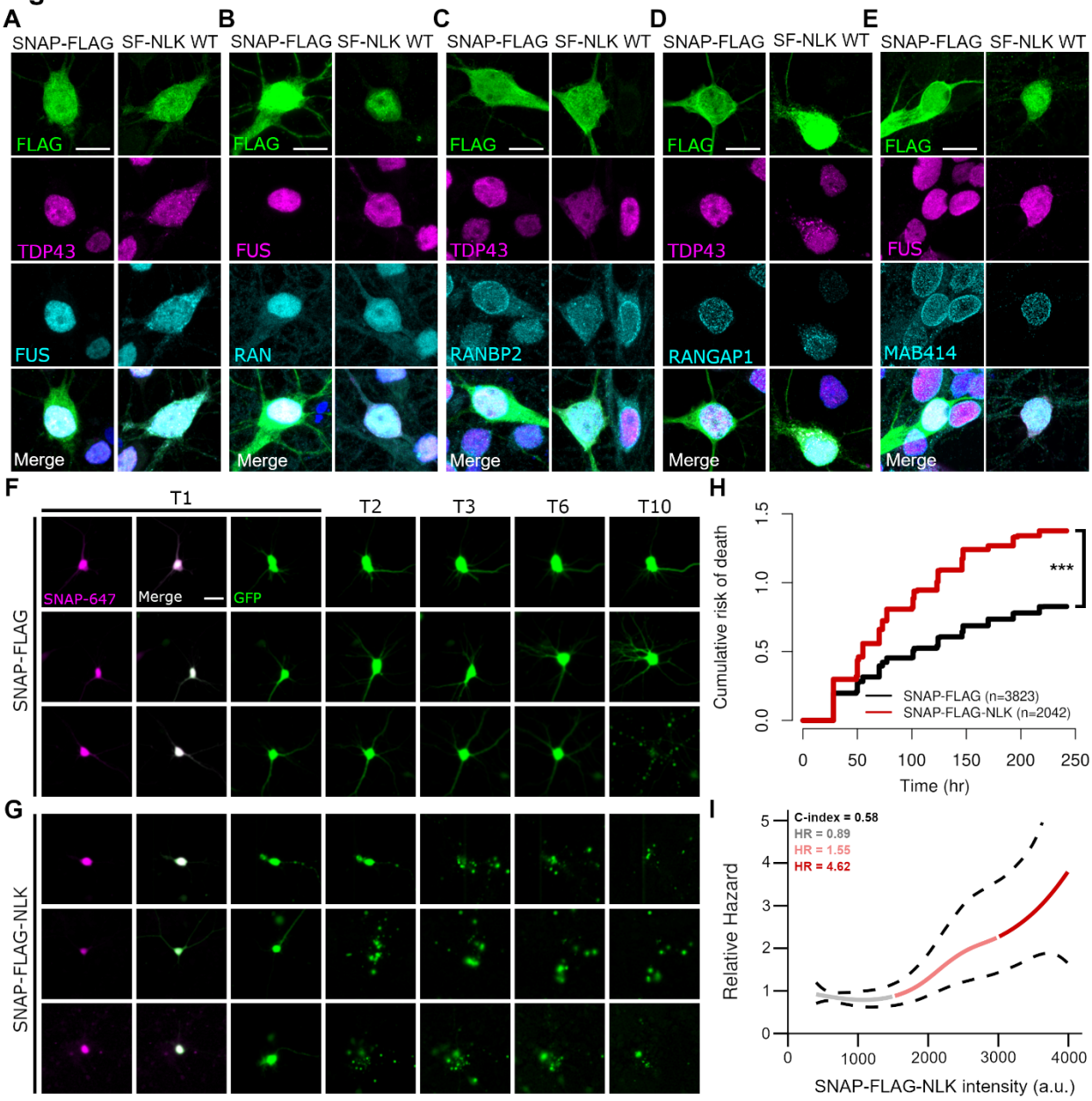

Figure 6. NLK overexpression disrupts nuclear import and is toxic in primary rat neurons. (**A**) Rodent primary cortical neurons were transfected with either SNAP-FLAG (SF; negative-control) or SNAP-FLAG-NLK (SF-NLK) followed by immunofluorescence using antibodies against FLAG and either TDP43, FUS, Ran, RanBP2, RanGAP1, and Mab414 while DNA was stained with Hoechst.Scale bar = 10 µm. (**B**) Rodent primary cortical neurons were co-transfected with plasmids

677 encoding either SF or SF-NLK and EGFP (survival marker), treated with SNAP-647 dye at T1 to
678 visualize SNAP-positive neurons, and tracked by longitudinal microscopy to determine neuron fate
679 (see methods). Scale bar = 20μm. (**C**) Cumulative Hazard plot showing the relative risk of death in
680 neurons that express either SF or SF-NLK. Hazard ratio = 1.616. ***p=1.494e-59. (**D**) Cox
681 proportional hazards model predicting relative hazard associated with different intensities of
682 SNAP-FLAG-NLK. Solid lines indicate the estimated hazard, with color gradients corresponding to
683 intensity levels: grey (low intensity), light red (medium intensity), and red (high intensity). Dashed
684 lines represent 95% confidence intervals for hazard estimates.

Figure 7

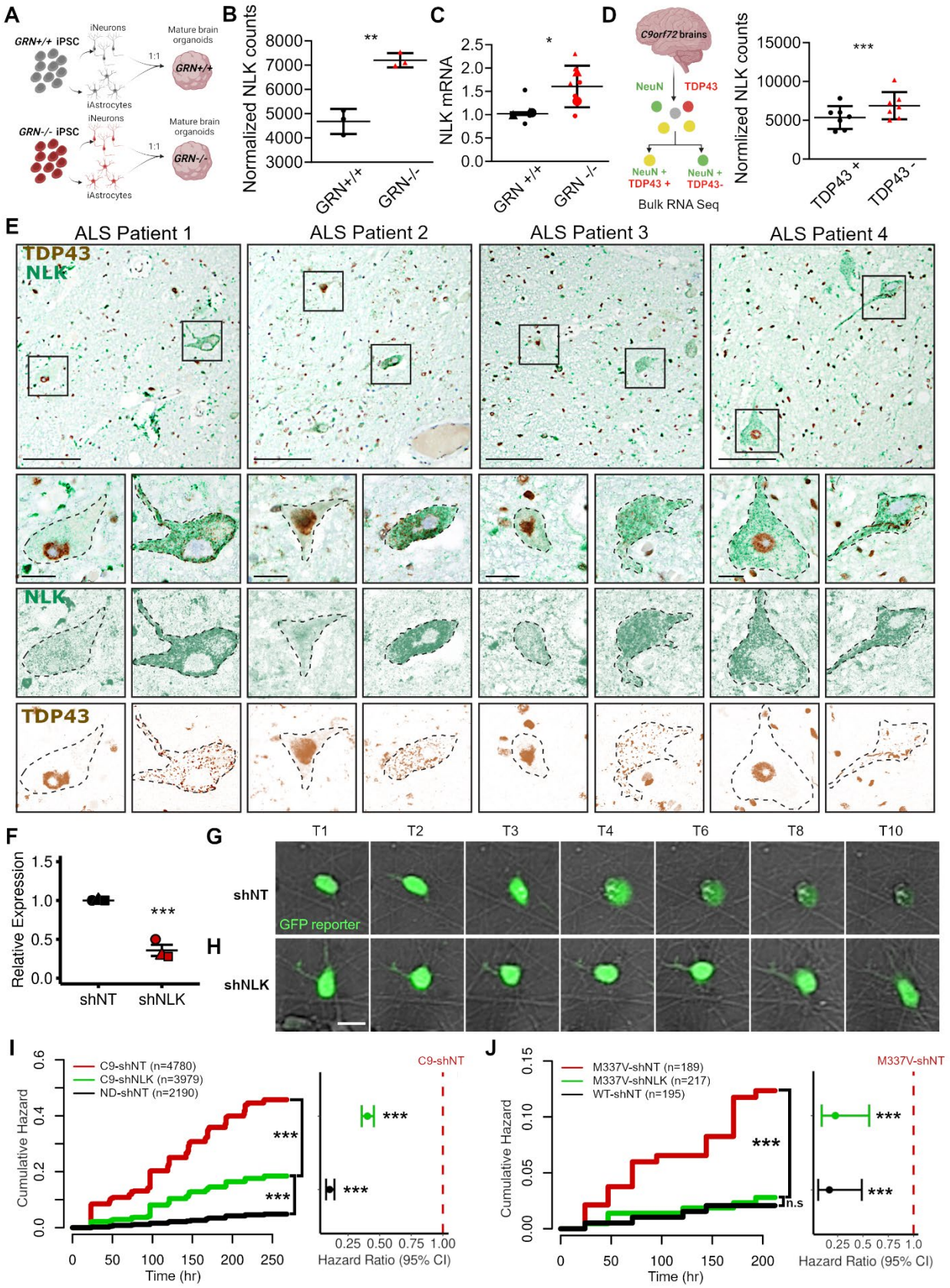
A
GRN+/+ iPSC
iNeurons
iAstrocytes
Mature brain organoids
1:1
GRN+/+
GRN-/- iPSC
GRN-/-
B
Normalized NLK counts
GRN+/+
GRN-/-
C
NLK mRNA
GRN +/+
GRN -/-
D
C9orf72 brains
NeuN
TDP43
NeuN + TDP43 +
NeuN + TDP43-
Bulk RNA Seq
Normlized NLK counts
TDP43 +
TDP43 -
E
ALS Patient 1
ALS Patient 2
ALS Patient 3
ALS Patient 4
TDP43
NLK
F
Relative Expression
shNT
shNLK
G
H
T1
T2
T3
T4
T6
T8
T10
GFP reporter
I
C9-shNT (n=4780)
C9-shNLK (n=3979)
ND-shNT (n=2190)
Cumulative Hazard
Time (hr)
Hazard Ratio (95% CI)
J
M337V-shNT (n=189)
M337V-shNLK (n=217)
WT-shNT (n=195)
n.s

685

686

687 **Figure 7. TDP43 pathology is associated with NLK overexpression in human model systems**
688 **and patient samples.** (**A**) Schematic of generation of mbOrgs. (**B**) Normalized NLK counts from
689 RNASeq performed on WT or GRN$^{-/-}$ mbOrgs. Line = mean, error bar = standard deviation. ** p< 0.01
690 (unpaired t-test with Welch's correction). (**C**) QPCR was performed on WT or GRN$^{-/-}$ mbOrgs (2
691 biological replicates, 3 technical replicates). Superplot of NLK levels normalized to GAPDH. Line =
692 mean, error bar = standard deviation. * p<0.05 (unpaired t-test with Welch's correction). (**D**) NLK
693 normalized counts from RNAseq performed on TDP positive and negative nuclei. Line = mean, error
694 bar = standard deviation. **** p<0.001 (Wald tests, corrected for multiple testing using the
695 Benjamini–Hochberg method). (**E**) Dual immunohistochemistry for NLK and TDP43, performed on
696 spinal cord tissue from four patients with sporadic ALS. Images deconvolved using FIJI. Upper
697 panels: scale bar 100 μm. Lower panels: scale bar 20 μm. (**F**) Quantitative real-time PCR of NLK
698 mRNA levels in iPSC derived neurons after transduction with lentivirus virus encoding either non-
699 targeting shRNA (shNT) or NLK shRNA (shNLK). Line = mean, error bar = standard error. *** p<
700 0.001 (unpaired t-test with Welch's correction). (**G**) Isogenic (WT) and mutant TDP43 (M337V) iPSC-
701 derived neurons were transduced with virus encoding either non targeting (NT) shRNA or NLK
702 shRNA followed by longitudinal microscopy to track neuron fate (see methods). Scale bar = 20 μm.
703 (**H**) Cumulative Hazard plot showing the relative risk of death in ND and C9 neurons that express
704 either shNT shRNA or shNLK (HR = 0.4, p<0.001). (**I**) Cumulative Hazard plot showing the relative
705 risk of death in WT and M337V neurons that express either Scramble shRNA or NLKshRNA. (HR =
706 0.23, p=0.0013).

707 **References**

708 1. Brown RH, and Al-Chalabi A. Amyotrophic Lateral Sclerosis. *N Engl J Med*.
709 2017;377(16):1602.
710 2. Tan RH, Ke YD, Ittner LM, and Halliday GM. ALS/FTLD: experimental models and reality.
711 *Acta Neuropathol*. 2017;133(2):177-96.
712 3. Neumann M, Sampathu DM, Kwong LK, Truax AC, Micsenyi MC, Chou TT, et al.
713 Ubiquitinated TDP-43 in frontotemporal lobar degeneration and amyotrophic lateral
714 sclerosis. *Science*. 2006;314(5796):130-3.
715 4. Alami NH, Smith RB, Carrasco MA, Williams LA, Winborn CS, Han SSW, et al. Axonal
716 transport of TDP-43 mRNA granules is impaired by ALS-causing mutations. *Neuron*.
717 2014;81(3):536-43.
718 5. Ling JP, Pletnikova O, Troncoso JC, and Wong PC. TDP-43 repression of nonconserved
719 cryptic exons is compromised in ALS-FTD. *Science*. 2015;349(6248):650-5.
720 6. Polymenidou M, Lagier-Tourenne C, Hutt KR, Huelga SC, Moran J, Liang TY, et al. Long pre-
721 mRNA depletion and RNA missplicing contribute to neuronal vulnerability from loss of TDP-
722 43. *Nat Neurosci*. 2011;14(4):459-68.
723 7. Tank EM, Figueroa-Romero C, Hinder LM, Bedi K, Archbold HC, Li X, et al. Abnormal RNA
724 stability in amyotrophic lateral sclerosis. *Nat Commun*. 2018;9(1):2845.
725 8. Takeuchi R, Toyoshima Y, Tada M, Shiga A, Tanaka H, Shimohata M, et al. Transportin 1
726 accumulates in FUS inclusions in adult-onset ALS without FUS mutation. *Neuropathol Appl*
727 *Neurobiol*. 2013;39(5):580-4.
728 9. Freibaum BD, Lu Y, Lopez-Gonzalez R, Kim NC, Almeida S, Lee KH, et al. GGGGCC repeat
729 expansion in C9orf72 compromises nucleocytoplasmic transport. *Nature*.
730 2015;525(7567):129-33.

731 10. Jovičić A, Mertens J, Boeynaems S, Bogaert E, Chai N, Yamada SB, et al. Modifiers of
732 C9orf72 dipeptide repeat toxicity connect nucleocytoplasmic transport defects to FTD/ALS.
733 *Nat Neurosci*. 2015;18(9):1226-9.
734 11. Zhang K, Donnelly CJ, Haeusler AR, Grima JC, Machamer JB, Steinwald P, et al. The C9orf72
735 repeat expansion disrupts nucleocytoplasmic transport. *Nature*. 2015;525(7567):56-61.
736 12. Thorpe CJ, and Moon RT. nemo-like kinase is an essential co-activator of Wnt signaling
737 during early zebrafish development. *Development*. 2004;131(12):2899-909.
738 13. Yasuda J, Tsuchiya A, Yamada T, Sakamoto M, Sekiya T, and Hirohashi S. Nemo-like kinase
739 induces apoptosis in DLD-1 human colon cancer cells. *Biochem Biophys Res Commun*.
740 2003;308(2):227-33.
741 14. Emami KH, Brown LG, Pitts TE, Sun X, Vessella RL, and Corey E. Nemo-like kinase induces
742 apoptosis and inhibits androgen receptor signaling in prostate cancer cells. *Prostate*.
743 2009;69(14):1481-92.
744 15. Tejwani L, Jung Y, Kokubu H, Sowmithra S, Ni L, Lee C, et al. Reduction of nemo-like kinase
745 increases lysosome biogenesis and ameliorates TDP-43-related neurodegeneration. *J Clin*
746 *Invest*. 2023;133(16).
747 16. Ju H, Kokubu H, Todd TW, Kahle JJ, Kim S, Richman R, et al. Polyglutamine disease toxicity
748 is regulated by Nemo-like kinase in spinocerebellar ataxia type 1. *J Neurosci*.
749 2013;33(22):9328-36.
750 17. Todd TW, Kokubu H, Miranda HC, Cortes CJ, La Spada AR, and Lim J. Nemo-like kinase is a
751 novel regulator of spinal and bulbar muscular atrophy. *Elife*. 2015;4:e08493.
752 18. Jiang M, Zhang X, Liu H, LeBron J, Alexandris A, Peng Q, et al. Nemo-like kinase reduces
753 mutant huntingtin levels and mitigates Huntington's disease. *Hum Mol Genet*.
754 2020;29(8):1340-52.

755 19. Brott BK, Pinsky BA, and Erikson RL. Nlk is a murine protein kinase related to Erk/MAP
756 kinases and localized in the nucleus. *Proc Natl Acad Sci U S A*. 1998;95(3):963-8.
757 20. Lee BJ, Cansizoglu AE, Süel KE, Louis TH, Zhang Z, and Chook YM. Rules for nuclear
758 localization sequence recognition by karyopherin beta 2. *Cell*. 2006;126(3):543-58.
759 21. Winton MJ, Igaz LM, Wong MM, Kwong LK, Trojanowski JQ, and Lee VM. Disturbance of
760 nuclear and cytoplasmic TAR DNA-binding protein (TDP-43) induces disease-like
761 redistribution, sequestration, and aggregate formation. *J Biol Chem*. 2008;283(19):13302-9.
762 22. Hisada-Ishii S, Ebihara M, Kobayashi N, and Kitagawa Y. Bipartite nuclear localization signal
763 of matrin 3 is essential for vertebrate cells. *Biochem Biophys Res Commun*.
764 2007;354(1):72-6.
765 23. Ederle H, Funk C, Abou-Ajram C, Hutten S, Funk EBE, Kehlenbach RH, et al. Nuclear egress
766 of TDP-43 and FUS occurs independently of Exportin-1/CRM1. *Sci Rep*. 2018;8(1):7084.
767 24. Pinarbasi ES, Cağatay T, Fung HYJ, Li YC, Chook YM, and Thomas PJ. Active nuclear import
768 and passive nuclear export are the primary determinants of TDP-43 localization. *Sci Rep*.
769 2018;8(1):7083.
770 25. Archbold HC, Jackson KL, Arora A, Weskamp K, Tank EM, Li X, et al. TDP43 nuclear export
771 and neurodegeneration in models of amyotrophic lateral sclerosis and frontotemporal
772 dementia. *Sci Rep*. 2018;8(1):4606.
773 26. Dormann D, Rodde R, Edbauer D, Bentmann E, Fischer I, Hruscha A, et al. ALS-associated
774 fused in sarcoma (FUS) mutations disrupt Transportin-mediated nuclear import. *EMBO J*.
775 2010;29(16):2841-57.
776 27. Görlich D, Vogel F, Mills AD, Hartmann E, and Laskey RA. Distinct functions for the two
777 importin subunits in nuclear protein import. *Nature*. 1995;377(6546):246-8.

778 28. Xing Z, Zhen Y, Chen J, Du M, Li D, Liu R, et al. KPNA2 Silencing, Regulated by E3 Ubiquitin
779 Ligase FBXW7, Alleviates Endothelial Dysfunction and Inflammation Through Inhibiting the
780 Nuclear Translocation of p65 and IRF3: A Possible Therapeutic Approach for
781 Atherosclerosis. *Inflammation*. 2023;46(6):2071-88.
782 29. Stewart M. Molecular mechanism of the nuclear protein import cycle. *Nat Rev Mol Cell Biol*.
783 2007;8(3):195-208.
784 30. Varjosalo M, Keskitalo S, Van Drogen A, Nurkkala H, Vichalkovski A, Aebersold R, et al. The
785 protein interaction landscape of the human CMGC kinase group. *Cell Rep*. 2013;3(4):1306-
786 20.
787 31. Mahajan R, Delphin C, Guan T, Gerace L, and Melchior F. A small ubiquitin-related
788 polypeptide involved in targeting RanGAP1 to nuclear pore complex protein RanBP2. *Cell*.
789 1997;88(1):97-107.
790 32. Saitoh H, Pu R, Cavenagh M, and Dasso M. RanBP2 associates with Ubc9p and a modified
791 form of RanGAP1. *Proc Natl Acad Sci U S A*. 1997;94(8):3736-41.
792 33. Matunis MJ, Coutavas E, and Blobel G. A novel ubiquitin-like modification modulates the
793 partitioning of the Ran-GTPase-activating protein RanGAP1 between the cytosol and the
794 nuclear pore complex. *J Cell Biol*. 1996;135(6 Pt 1):1457-70.
795 34. Duan L, Zaepfel BL, Aksenova V, Dasso M, Rothstein JD, Kalab P, et al. Nuclear RNA binding
796 regulates TDP-43 nuclear localization and passive nuclear export. *Cell Rep*.
797 2022;40(3):111106.
798 35. Buratti E, and Baralle FE. Characterization and functional implications of the RNA binding
799 properties of nuclear factor TDP-43, a novel splicing regulator of CFTR exon 9. *J Biol Chem*.
800 2001;276(39):36337-43.

801 36. Flores BN, Li X, Malik AM, Martinez J, Beg AA, and Barmada SJ. An Intramolecular Salt Bridge
802 Linking TDP43 RNA Binding, Protein Stability, and TDP43-Dependent Neurodegeneration.
803 *Cell Rep*. 2019;27(4):1133-50.e8.
804 37. Pérez-Berlanga M, Wiersma VI, Zbinden A, De Vos L, Wagner U, Foglieni C, et al. Loss of
805 TDP-43 oligomerization or RNA binding elicits distinct aggregation patterns. *EMBO J*.
806 2023;42(17):e111719.
807 38. Ilik İ, Malszycki M, Lübke AK, Schade C, Meierhofer D, and Aktaş T. SON and SRRM2 are
808 essential for nuclear speckle formation. *Elife*. 2020;9.
809 39. Imamura K, Imamachi N, Akizuki G, Kumakura M, Kawaguchi A, Nagata K, et al. Long
810 noncoding RNA NEAT1-dependent SFPQ relocation from promoter region to paraspeckle
811 mediates IL8 expression upon immune stimuli. *Mol Cell*. 2014;53(3):393-406.
812 40. Mitrea DM, Cika JA, Guy CS, Ban D, Banerjee PR, Stanley CB, et al. Nucleophosmin
813 integrates within the nucleolus via multi-modal interactions with proteins displaying R-rich
814 linear motifs and rRNA. *Elife*. 2016;5.
815 41. Arrasate M, Mitra S, Schweitzer ES, Segal MR, and Finkbeiner S. Inclusion body formation
816 reduces levels of mutant huntingtin and the risk of neuronal death. *Nature*.
817 2004;431(7010):805-10.
818 42. Barmada SJ, Serio A, Arjun A, Bilican B, Daub A, Ando DM, et al. Autophagy induction
819 enhances TDP43 turnover and survival in neuronal ALS models. *Nat Chem Biol*.
820 2014;10(8):677-85.
821 43. Barmada SJ, Ju S, Arjun A, Batarse A, Archbold HC, Peisach D, et al. Amelioration of toxicity
822 in neuronal models of amyotrophic lateral sclerosis by hUPF1. *Proc Natl Acad Sci U S A*.
823 2015;112(25):7821-6.

824 44. Miller J, Arrasate M, Shaby BA, Mitra S, Masliah E, and Finkbeiner S. Quantitative
825 relationships between huntingtin levels, polyglutamine length, inclusion body formation,
826 and neuronal death provide novel insight into huntington's disease molecular
827 pathogenesis. *J Neurosci*. 2010;30(31):10541-50.
828 45. Strong MJ, Abrahams S, Goldstein LH, Woolley S, Mclaughlin P, Snowden J, et al.
829 Amyotrophic lateral sclerosis - frontotemporal spectrum disorder (ALS-FTSD): Revised
830 diagnostic criteria. *Amyotroph Lateral Scler Frontotemporal Degener*. 2017;18(3-4):153-74.
831 46. de Majo M, Koontz M, Marsan E, Salinas N, Ramsey A, Kuo YM, et al. Granulin loss of
832 function in human mature brain organoids implicates astrocytes in TDP-43 pathology. *Stem*
833 *Cell Reports*. 2023;18(3):706-19.
834 47. DeJesus-Hernandez M, Mackenzie IR, Boeve BF, Boxer AL, Baker M, Rutherford NJ, et al.
835 Expanded GGGGCC hexanucleotide repeat in noncoding region of C9ORF72 causes
836 chromosome 9p-linked FTD and ALS. *Neuron*. 2011;72(2):245-56.
837 48. Morita M, Al-Chalabi A, Andersen PM, Hosler B, Sapp P, Englund E, et al. A locus on
838 chromosome 9p confers susceptibility to ALS and frontotemporal dementia. *Neurology*.
839 2006;66(6):839-44.
840 49. McMillan M, Gomez N, Hsieh C, Bekier M, Li X, Miguez R, et al. RNA methylation influences
841 TDP43 binding and disease pathogenesis in models of amyotrophic lateral sclerosis and
842 frontotemporal dementia. *Mol Cell*. 2023;83(2):219-36.e7.
843 50. Boeynaems S, Bogaert E, Michiels E, Gijselinck I, Sieben A, Jovičić A, et al. Drosophila
844 screen connects nuclear transport genes to DPR pathology in c9ALS/FTD. *Sci Rep*.
845 2016;6:20877.

846 51. Hutten S, Flotho A, Melchior F, and Kehlenbach RH. The Nup358-RanGAP complex is
847 required for efficient importin alpha/beta-dependent nuclear import. *Mol Biol Cell*.
848 2008;19(5):2300-10.
849 52. Hong AW, Meng Z, Yuan HX, Plouffe SW, Moon S, Kim W, et al. Osmotic stress-induced
850 phosphorylation by NLK at Ser128 activates YAP. *EMBO Rep*. 2017;18(1):72-86.
851 53. Yuan HX, Wang Z, Yu FX, Li F, Russell RC, Jewell JL, et al. NLK phosphorylates Raptor to
852 mediate stress-induced mTORC1 inhibition. *Genes Dev*. 2015;29(22):2362-76.
853 54. Cargnello M, and Roux PP. Activation and function of the MAPKs and their substrates, the
854 MAPK-activated protein kinases. *Microbiol Mol Biol Rev*. 2011;75(1):50-83.
855 55. Peters S, Zitzelsperger E, Kuespert S, Iberl S, Heydn R, Johannesen S, et al. The TGF-β
856 System As a Potential Pathogenic Player in Disease Modulation of Amyotrophic Lateral
857 Sclerosis. *Front Neurol*. 2017;8:669.
858 56. Zhang N, Westerhaus A, Wilson M, Wang E, Goff L, and Sockanathan S. Physiological
859 regulation of neuronal Wnt activity is essential for TDP-43 localization and function. *EMBO*
860 *J*. 2024.
861 57. Ke H, Masoumi KC, Ahlqvist K, Seckl MJ, Rydell-Törmänen K, and Massoumi R. Nemo-like
862 kinase regulates the expression of vascular endothelial growth factor (VEGF) in alveolar
863 epithelial cells. *Sci Rep*. 2016;6:23987.
864 58. Kortenjann M, Nehls M, Smith AJ, Carsetti R, Schüler J, Köhler G, et al. Abnormal bone
865 marrow stroma in mice deficient for nemo-like kinase, Nlk. *Eur J Immunol*.
866 2001;31(12):3580-7.
867 59. Liu R, Khalil H, Lin SJ, Sargent MA, York AJ, and Molkentin JD. Nemo-Like Kinase (NLK) Is a
868 Pathological Signaling Effector in the Mouse Heart. *PLoS One*. 2016;11(10):e0164897.

869 60. Weskamp K, Tank EM, Miguez R, McBride JP, Gómez NB, White M, et al. Shortened TDP43
870 isoforms upregulated by neuronal hyperactivity drive TDP43 pathology in ALS. *J Clin Invest*.
871 2020;130(3):1139-55.
872 61. Miyaoka Y, Chan AH, Judge LM, Yoo J, Huang M, Nguyen TD, et al. Isolation of single-base
873 genome-edited human iPS cells without antibiotic selection. *Nat Methods*. 2014;11(3):291-
874 3.
875 62. Barmada SJ, Skibinski G, Korb E, Rao EJ, Wu JY, and Finkbeiner S. Cytoplasmic
876 mislocalization of TDP-43 is toxic to neurons and enhanced by a mutation associated with
877 familial amyotrophic lateral sclerosis. *J Neurosci*. 2010;30(2):639-49.
878 63. Malik AM, Miguez RA, Li X, Ho YS, Feldman EL, and Barmada SJ. Matrin 3-dependent
879 neurotoxicity is modified by nucleic acid binding and nucleocytoplasmic localization. *Elife*.
880 2018;7.
881 64. Weskamp K, Safren N, Miguez R, and Barmada S. Monitoring Neuronal Survival via
882 Longitudinal Fluorescence Microscopy. *J Vis Exp*. 2019(143).
883 65. Pfaffl MW. A new mathematical model for relative quantification in real-time RT-PCR.
884 *Nucleic Acids Res*. 2001;29(9):e45.
885 66. Ishitani T, Hirao T, Suzuki M, Isoda M, Ishitani S, Harigaya K, et al. Nemo-like kinase
886 suppresses Notch signalling by interfering with formation of the Notch active
887 transcriptional complex. *Nat Cell Biol*. 2010;12(3):278-85.
888 67. Fu SC, Fung HYJ, Cağatay T, Baumhardt J, and Chook YM. Correlation of CRM1-NES affinity
889 with nuclear export activity. *Mol Biol Cell*. 2018;29(17):2037-44.
890 68. CVAT.ai, and Corporation. Computer Vision Annotation Tool (CVAT) (v2.11.2).
891 doi:10.5281/zenodo.10807509.

892 69. Cao MC, and Scotter EL. Transcriptional targets of amyotrophic lateral
893 sclerosis/frontotemporal dementia protein TDP-43 - meta-analysis and interactive
894 graphical database. *Dis Model Mech*. 2022;15(9).